Acid treated Ce modified birnessite–type MnO2 for ozone decomposition at low temperature: Effect of nitrogen containing co-pollutants and water

Grece Abdallah, Rim Bitar, Savita Kaliya Perumal Veerapandian, Jean-Marc Giraudon, Nathalie de Geyter, Rino Morent, Jean-Francois Lamonier

Version of Record: https://www.sciencedirect.com/science/article/pii/S0169433221022935
Manuscript_44034d0fdedad5d42ee5bfd2c714fb0e

Acid treated Ce modified birnessite–type MnO_2 for ozone decomposition at low temperature: effect of nitrogen containing co-pollutants and water

Grêce Abdallah[1,2], Rim Bitar[2], Savita Kaliya Perumal Veerapandian[2], Jean-Marc Giraudon[1]*, Nathalie De Geyter[2], Rino Morent[2] and Jean-François Lamonier[1]

[1] Univ. Lille, CNRS, Centrale Lille, Univ. Artois, UMR 8181-UCCS-Unité de Catalyse et Chimie du Solide, F-59000 Lille, France

[2] Research Unit Plasma Technology (RUPT), Department of Applied Physics, Faculty of Engineering and Architecture, Ghent University, Sint-Pietersnieuwstraat 41 (B4), 9000 Ghent, Belgium

* Correspondence: jean-marc.giraudon@univ-lille.fr

Abstract

In this study, HNO_3 treated Ce modified birnessite–type MnO_2 (Ce_xMn-AT; x = 0.01,0.1,0.2,0.5) have been designed for decomposition of ozone at low temperature (20-40 °C) in the absence or presence of nitrogen containing co-pollutants and water. The best catalyst $Ce_{0.01}Mn$-AT exhibits stable ozone conversion of 94 % in nearly dry air (300 ppm of ozone, RH = 0.7 %, GHSV = 1200 L/(g.h), 20 °C) in the presence of N_2O_5/HNO_3 pollutants. However, the ozone conversion drops to 64 % for the undoped catalyst showing the beneficial role of cerium. Additionally, the $Ce_{0.1}Mn$-AT catalyst shows a stable ozone conversion of 91 % after 5 h on stream in moist air (RH = 30%, 30 °C) in the same operating conditions as before. The high tolerance of the best acid-treated catalysts to co-pollutants and water can be explained by the high density of acid sites and oxygen vacancies which facilitate the adsorption and decomposition of ozone and allow to minimize the amount of nitrogen containing adspecies which can affect the catalytic performances for ozone decomposition.

Keywords: Ozone decomposition: nitrogen containing pollutant tolerant: water tolerant: cerium modified birnessite: acid treatment

1. Introduction

Tropospheric, or ground-level ozone (O_3), sometimes referred to as bad ozone, is formed in the lower atmosphere. O_3 is not emitted directly into the air but is derived from precursors (nitrogen oxides (NOx) and volatile organic compounds (VOC)) mainly emitted by human activities and flora, in the presence of sunlight [1]. Ozone peaks therefore appear when there is a lot of sunshine and in anticyclonic conditions. Ground-level ozone is a very harmful air pollutant, both for humans and the environment [2] and increased ground-level ozone has become the main cause of photochemical smog. Ozone is one of six common air pollutants identified in the Clean Air Act and is classified as "criteria air pollutant" because they can harm our health [3]. In order to eliminate ozone pollution in non-compliant areas, removal effective strategies must be implemented.

Currently, different processes for ozone removal are studied, including absorption [4], adsorption [5] and catalytic decomposition [6–8]. Among these methods, ozone catalytic decomposition has received particular attention because of its high efficiency even under mild operating conditions (low temperature). Transition metal oxides, especially manganese-based oxides, have been widely studied because of their low cost and high efficiency due to the presence of large amounts of surface oxygen vacancies [9,10]. However, the efficiency of manganese oxide catalysts is reduced in the course of the reaction and a deactivation over time is observed. This deactivation is generally explained by an adsorption competition between ozone and water molecules (also present in the gas stream) which leads to a blockage of the active sites [11]. The moisture resistance of manganese oxides could be enhanced by adding noble metals [12], removing the residual surface acid ions [13] or treating with nitric acid [14]. Nitric acid-treated birnessite-type MnO_2 has been demonstrated to be an efficient and hydrophobic catalyst for humid ozone decomposition [15]. The addition of cerium element to manganese oxides could be also an efficient way in preventing the deactivation of

the catalysts under high humidity conditions. Indeed, previous work has revealed that cerium oxide is resistant to water. In particular, CeO_2 (111) has been proved to be a catalytically active crystal facet for the hydrolysis reaction [16]. The presence of CeO_2 in the catalyst could therefore prevent the strong association between water and vacant oxygen sites. Furthermore, the addition of cerium in MnO_x may contribute to a significant improvement of the catalytic performance in the ozone decomposition reaction owing to (i) an increase in surface area, (ii) a decrease in crystallinity, and (iii) a larger amount of surface oxygen vacancies [17]. It is believed that the oxygen transfer between Ce^{4+} and Ce^{3+} species on the surface of the catalysts allows abundant oxygen species storage and leads to superior redox properties compared to those obtained with simple manganese oxides [18,19]. The introduction of Ce also leads to an electron transfer between manganese and cerium which improves the redox capacity of the material and consequently its catalytic performance [18].

Moreover, the emergence of future aeronautical standards requires the development of novel catalysts for the ozone decomposition reaction that are highly active and stable at low temperatures in the presence of water but also in the presence of other molecules. It is particularly important to estimate the sensitivity of these new catalysts to nitrogen oxides, which are mainly emitted into the atmosphere by diesel engines [20]. Such nitrogen containing pollutants can be present when O_3 is generated by DBD non-thermal plasma [21–24]. An inhibiting effect of NO_x on ozone decomposition is observed in the presence of several catalyst compositions such as Ni-Mn spinel [25] and activated carbon [26]. Very recently, ozone decomposition has been investigated in the presence of NO_x at low temperature over a commercial Pd/Al_2O_3. NO_x species have been shown to significantly poison the catalyst, resulting in a significant decrease of ozone conversion over time on stream [21].

Herein, a series of novel acid treated Ce_xMn catalysts have been successfully synthesized. The nitric acid treatment has been performed on Ce modified birnessites. These catalysts have been tested in comparison with the non-acid treated catalysts in non-thermal plasma generated ozone decomposition at low temperature in nearly dry and moist air. The presence of nitrogen containing contaminants has been assessed by the generation of ozone from air using a Non thermal plasma with a negative direct current corona discharge. The structure-performance relationship has been established and the role of the acid treatment and of the promotion role of cerium on ozone decomposition has been discussed considering the nitrogen gaseous species.

2. Material and methods

2.1. Catalyst preparation

Modified birnessite type MnO_2 were prepared following a redox method inspired from the work of Händel *et al*. [27]. Typically, 4.0 g (25.3 mmol) of $KMnO_4$ (Fluka, ≥ 99 %) were dissolved into 400 mL of distilled water under stirring (350 rpm). Appropriate amount of $Ce(NO_3)_3.6H_2O$ (Alfa Aesar; purity ≥ 99.5 %) was dissolved concomitantly with $KMnO_4$. 4 mL (22.54 mmol) of sodium lactate ($NaC_3H_5O_3$; 50 % w/w obtained from a Fisher Chemical solution 60 % w/w) was added dropwise to the aqueous $KMnO_4$ solution. The resulting brown suspension was stirred for 2 h. After centrifugation (4000 rpm for 20 min), the collected brown precipitate was washed 2 times (25 mL of distilled water each time) and finally dried in an oven at 40 °C for 48 h to give a black powder. Subsequently, the samples were treated with a 0.2 M HNO_3 solution (VWR. 68%) in a beaker with a solid to liquid mass ratio of 1/20 for 6 hours at 50 °C under vigorous stirring (500 rpm). Then, the resulting black suspension was filtered and intensively washed with deionized water until the pH of the eluate was ~7.0. The samples were labelled Mn-B-AT (sample without cerium, B: Birnessite) and Ce_xMn-AT (where x is the Ce/Mn atomic ratio of 0.01, 0.1 0.2 and 0.5), AT referring to acid treatment.

2.2. Catalyst characterization

X-ray diffraction patterns (XRD) were recorded on a D8 Advanced Bruker AXS diffractometer equipped with Cu $K_{\alpha 1}$ monochromatic radiation source (λ = 1.5406 Å) which operated at 40 kV and 40 mA. The X-ray diffraction patterns were recorded in the range of 2θ of 5 °- 80 °, step size : 0.02 º in 2θ, time per step = 1s.

N_2 physisorption isotherms were recorded at -196 °C using a gas sorption analyzer TriStar II 3020 from Micromeritics. Prior to analysis, the samples were outgassed at 100 °C for 4 h

under dynamic vacuum. The specific surface area was determined according to Brunauer-Emmett-Teller (BET) method. The total pore volume V_p was determined at $P/P_0 = 0.99$. The Barret-Joyner-Halenda (BJH) equation was used to estimate the pore size distributions (PSD) from the desorption isotherm.

The elemental analysis was performed by Inductively Coupled Plasma - Optic Emission Spectroscopy 720-ES ICP-OES.

Transmission electron microscopy (TEM) characterization was performed using a TECNAI TEM operated at 200 kV. The prepared powders were deposited onto a carbon-coated copper grid for TEM observation.

TGA were carried out on 5 mg of sample in dry flowing air (100 mL/min) with a heating rate of 10 °C/min up to 800 °C using a DSC-TGA SDT 2960 of TA Instrument.

Pyridine adsorption experiments were performed using an *in situ* IR quartz cell equipped with KBr window attached to a vacuum system (dynamic vacuum better than 10^{-7} mbar). FTIR measurements were carried out using a Nicolet protege 460 spectrometer equipped with a MCT detector at a spectral resolution of 2 cm^{-1}. The sample placed as a self-supported sample disk (16 mm in diameter, S = 2.01 cm^2) in the IR cell was activated at 105 °C in vacuum (5 °C/min). Adsorption of pyridine (C_5H_5N, Acros Organics, 99.5%, dried over 3A molecular sieve) was carried out until pressure equilibrium (1.2 mbar at 105 °C). Most physisorbed pyridine molecules were subsequently removed by evacuation at 105 °C in vacuum for 30 min. The FTIR spectra were then acquired at 105 °C. All recorded FTIR spectra were normalized to a mass of 10 mg.

H_2-Temperature Programmed Reduction (H_2-TPR) experiments were performed on a Micromeritics Autochem II 2920 instrument. About 50 mg of sample was placed in a U-shaped tubular quartz reactor and pre-treated in flowing Ar at 150 °C for 1 h followed by

cooling. The sample was reduced in 5 vol. % H_2 in Ar with a flow rate of 50 mL/min. The temperature was increased from 25 °C to 800 °C with a heating rate of 10 °C/min.

X-ray photoelectron spectroscopy (XPS) experiments were performed using an AXIS Ultra DLD Kratos spectrometer equipped with a monochromatic aluminum source (Al K_α = 1486.7 eV) and charge compensation gun. The C 1s peak at 284.8 eV was taken as binding energy (BE) reference. CasaXPS software was used to process the XPS data. The Mn $2p_{3/2}$ analysis was performed considering Biesinger's procedure [28] consisting of representing the Mn^{3+} component by one peak and the Mn^{4+} component by six peaks. The FWMH of 1.2 eV was adapted to the energy bandwidth of 40 eV. The BE of the Mn^{4+} peak with the lowest BE was allowed to vary of ± 0.2 eV and the difference in BE with the Mn^{3+} peak was set at 1.0 eV. The Mn average oxidation state (AOS) was estimated from the empirical equation AOS = 8.956 - 1.126 × ΔE [29–32] where ΔE represented the BE separation between the two Mn 3s peaks. Quantification of the data was performed taking into account the K 2p, O 1s, Mn 2p, N 1s and Ce 4d core levels.

ToF-SIMS data were acquired using a ToF-SIMS5 spectrometer (ION-TOF GmbH Germany) equipped with a bismuth liquid metal ion gun (LMIG). The powders were crushed using an agate mortar and pestle and the standard tablets were prepared using a press machine. The samples were bombarded with a pulsed Bi_3^+ primary ion beam (25 keV, 0.25 pA) rastered over a 100 µm x 100 µm surface area (128 x 128 pixels and 100 scans). The total fluence did not amount up to 10^{12} ions/cm^2 ensuring static conditions. Charge effects were compensated by means of a 20 eV pulsed electron flood gun. With a cycle time of 200 µs, data were collected over a mass range m/z = 0-3500 for both positive and negative secondary ions. The fragments were identified by their exact mass, coupled with the appropriate intensities for the expected isotope pattern. The mass resolution m/Δm at m/z = 55 for Mn^+ was 5000.

2.3. Catalytic activity test

2.3.1. Description of the set-up

The Non thermal plasma (NTP) set-up consisted of three main parts: (i) the gas supply system, (ii) the reactor system and (iii) the gas analysis system which were described elsewhere [33]. The flow of dry air (ALPHAGAZ 1) was controlled by mass flow controllers (MFC) (Bronkhorst, El Flow*).* The reactor system consisted of two reactors placed in series: the NTP reactor and the catalytic reactor positioned downstream of the NTP reactor. The NTP reactor was a negative DC (direct current) corona-glow discharge reactor with a 10 pin-to-plate electrode configuration [34]. The discharge was powered with a 30 kV/20 mA DC power supply (Technix, SR40-R-1200) and generated at atmospheric pressure and room temperature. The catalytic reactor was a quartz tubular fixed bed reactor (i.d.: 20 mm). The gas analysis system consisted of a FTIR spectrometer (Bruker, Vertex 70). The FTIR gas cell equipped with ZnSe cell window (45 mm diameter) was used with a 20 cm optical path length.

2.3.2. Experimental procedure

Unless otherwise stated, the conditions were as followed. About 50 mg of catalyst was diluted with inert SiC (1g) and kept at 20 °C. A feed gas with a total flow rate of 1 L/min consisting of 300 ppm of O_3 diluted in synthesized air (20 % O_2/N_2; ALPHAGAZ 1) was flowed through the catalytic bed consisting in a GHSV of 1200 L/(g_{cat}.h). In the presence of moist air (RH = 30 %; water generated downstream the NTP reactor) the temperature was kept at 30 °C or 40 °C. In any case the downstream gas was analyzed by FTIR. The FTIR spectra were obtained by averaging 10 scans (data collection of 30 s) at a resolution of 4 cm^{-1}. O_3 conversion was defined as the ratio of the difference between inlet and outlet O_3 concentrations to the inlet O_3

concentration which were obtained from FTIR band integration between 1000 and 1050 cm $^{-1}$. The catalysts after test were labelled with an additional suffix which was $–O_3$ for reaction performed in nearly dry air and $–O_3$-H-X (H: Humidity; X: temperature in ° C) when performed at RH = 30 %.

3. Results and discussion

3.1. Catalytic tests for ozone decomposition

The decomposition of 300 ppmv of O_3 generated from air at 20 °C as a function of time over the acid-treated catalysts is shown in Fig. 1. The acid-treated catalysts are very active in the early stages of the reaction and deactivate to varying extents (Fig.1). While the undoped acid treated catalyst Mn-B-AT deactivates strongly within the first four hours to reach a stable conversion of O_3 amounting to 64 % after 5 h, the $Ce_{0.01}$Mn-AT catalyst exhibits a constant conversion of O_3 of 94 % after 2 h on stream. For higher cerium content, the O_3 conversion declines nearly linearly with time for $Ce_{0.1}$Mn-AT and $Ce_{0.2}$Mn-AT to reach final values of 83 % and 76 %, respectively. A further increase in Ce content to 0.5 leads to O_3 conversion even lower than the undoped material of 33 %. This is mainly attributed to the decrease of Mn oxide content which constitutes the effective constituent of the catalytic reaction.

Besides, it is worthy to mention that if ozone is generated from O_2 diluted in Ar, 100 % O_3 conversion is observed over time on $Ce_{0.01}$Mn while a conversion of only 19 % is reached after 5 h on stream in O_2 diluted in nitrogen.

Fig. 1. O_3 conversion (O_3 inlet concentration: 300 ppm) vs time in nearly dry air, 20 °C on the acid-treated catalysts, GHSV = 1200 L/(g.h.)

These results suggest that the decrease in ozone conversion can be related to the formation of nitrogen containing pollutants in the plasma discharge in the presence of nitrogen in air as

previously reported in the literature [35]. The catalytic decomposition of ozone generated from air has also been investigated on the two best catalysts, namely $Ce_{0.01}Mn$-AT and $Ce_{0.1}Mn$-AT, at 40 °C in moist air (RH = 30 %) to examine their moisture tolerance. As shown in Fig. 2a the O_3 conversion increases strongly in the first 15 minutes in any case to reach after that period about 100 % and 96 % before to stabilize after 5 h at 96 % and 98 % for $Ce_{0.01}Mn$-AT and $Ce_{0.1}Mn$-AT, respectively. Even at 30 °C, the $Ce_{0.1}Mn$-AT catalyst exhibits again a high O_3 conversion of 91 % (Fig. 2b).

Fig. 2. O_3 conversion vs time on the acid treated catalysts (O_3 inlet concentration: 300 ppm, GHSV = 1200 L/(g.h.)) (a) in moist air RH = 30 %; 40 °C; (b) in moist air RH = 30 %; 30 °C.

Overall, minimization of the catalyst deactivation for ozone decomposition in air in the presence of traces of nitrogen containing species (as seen below) and water can be achieved by performing an acid treatment on the cerium modified MnO_2 catalysts. Additionally, the acid-treated $Ce_{0.01}Mn$ and $Ce_{0.1}Mn$ catalysts show remarkable catalytic performances for O_3 decomposition at RH of 30 % in the presence of nitrogen pollutants.

3.2. Gas phase characterization by FTIR

To assess the involvement of related nitrogen containing species in the activity decrease for O_3 decomposition the formation of gaseous species in the plasma discharge (PD) in the presence of air with low humidity (RH = 0.7 %) has been evaluated by FTIR and their temporal evolutions have been monitored at the outlet of the catalyst reactor in the course of the reaction for $Ce_{0.01}Mn$-AT as shown in Fig. 3, respectively. A typical FTIR spectrum at the inlet of the catalyst reactor (Inlet CR) shows bands at 2223 cm^{-1}, 1716 cm^{-1} and 1321 cm^{-1} assigned to N_2O, N_2O_5 and HNO_3, respectively, along with those at 2111 cm^{-1} and 1056 cm^{-1} attributed to O_3. To sum up, the NTP processed air allows the formation of N_2O, N_2O_5 and HNO_3 as nitrogen gaseous pollutants along with the formation of O_3 in the PD. As the relative

content of N_2O is unaffected by post-plasma catalysis, a small uptake of N_2O_5 and HNO_3 is observed only after 1 h.

In the presence of humidity, the FTIR spectrum of the inlet gaseous stream is significantly affected (Fig. 4). N_2O_5 is no longer observed while the band intensity ascribed to HNO_3 is enhanced. Additionally, some broad bands at 1409 cm^{-1} and 1477 cm^{-1} are now observed whose assignations are currently unclear. Besides, the strong band at 1627 cm^{-1} has been assigned to adding water. N_2O_5 reacts with H_2O to give HNO_3. Interestingly, the release of CO_2 in the early stages of the reactions can be linked to the destruction of some surface carbonate species at the catalyst surface of $Ce_{0.01}$Mn-AT. Consequently, the activation period of the catalyst can be partly explained by a progressive recovery of active sites poisoned by carbonate like species. It is worthwhile to note that the distribution of the nitrogen containing species keeps rather unchanged in the course of the reaction.

Fig. 3. Temporal evolution of the gas phase species for O_3 decomposition in air (RH~0.7 %) over $Ce_{0.01}$Mn-AT

Fig. 4. Temporal evolution of the gas phase species for O_3 decomposition in moist air (RH~30 %) over $Ce_{0.01}$Mn-AT

3.3. Characterization studies of the acid-treated catalysts

The X-ray diffraction pattern of Mn-B-AT which exhibits three broad peaks of low intensity centered at 12.2 °, 37.0 ° and 66.2 ° (Fig. 5) can be consistent with the formation of a related disordered birnessite [36]. This result suggests the formation of a layered structure with coexisting amorphous state domains. Besides, the diffraction peaks become even less resolved as cerium is added. At the highest doping ratio of 0.5 only a very broad peak of low intensity at about 30 ° is observed due to cubic CeO_2 phase (JCPDS No.00-034-0394) which implies an extensive destruction of the crystallized layered structure.

Fig. 5. XRD patterns of the fresh acid-treated samples

The results of elemental analysis performed by ICP-EOS are given in Table 1. For Mn-B-AT it is observed a K/Mn atomic ratio of 0.065 consistent with the value of 0.05 obtained by Liu *et al.* [15] for an acid-treated birnessite MnO_2 which is substantially lower than for a conventional birnessite (~ 0.26). The loss of K^+ is consistent with K^+/H^+ exchange at the interlayer position as already pointed out [10]. While this K/Mn ratio is poorly affected by a low loading of cerium, it markedly decreases with increasing cerium nominal content. This can be explained by an increase amount of leached K^+ resulting from partial substitution of K^+ by H^+ and/or Ce^{4+}. Besides, the Ce/Mn ratio is consistent with the nominal one for the lowest doping ratio while a two-fold decrease is observed for higher doping ratio (Ce/Mn: 0.1, 0.2). Such higher release of cerium could be correlated with different speciations of Ce in the material.

Table 1
Chemical composition, textural and redox properties of the fresh acid-treated samples

The HRTEM images of the $Ce_{0.1}$Mn-AT sample are given in Fig. 6. In agreement with XRD results, large amorphous areas coexist with crystallized regions. Blurred stacked layers of less than 5 nm are observed attesting of the layered structure of the material. The lattice spacing of 0.71 nm has been assigned to the (001) plane of the birnessite. In the crystallized regions, it is observed the (111) lattice planes of CeO_2 with lattice spacing of 0.31 nm. The formation of such an interface structure has been recognized as to promote Ce- -Mn interactions allowing the generation of plenty of oxygen vacancies, which might improve the mobility of the adsorbed and lattice oxygen species [37–42].

Fig. 6. HRTEM images of $Ce_{0.1}$Mn-AT

N_2 physisorption isotherms are shown in Fig. 7a. Specific surface area (S_{BET}) as well as pore volume V_p values are compared in Table 1. All catalysts exhibit a type IV isotherm profile with a hysteresis loop in line with a mesoporous structure. High S_{BET} (280 - 385 m^2/g),

important V_p (0.25 - 0.65 cm^3/g) and a small mean pore size D_p in the range (Fig. 7b : 3.8 - 6.0 nm) are obtained which are known to be beneficial for O_3 decomposition [17].

Fig. 7. (a) N_2 adsorption-desorption isotherms and (b) pore size distribution of the fresh acid-treated samples

The reducibility of the samples has been evaluated by H_2-TPR (Fig. 8). The H_2-TPR traces of the acid-treated Ce_xMn oxides (x = 0-0.2) samples can be divided into 4 components α, β, γ and δ. While the α consumption is linked to the removal of surface oxygen species, the other components are related to the near surface and bulk oxygen removal. As compared to the undoped sample, the addition of Ce decreases the onset reduction temperature, increases the relative β consumption while the γ and δ peaks move to higher temperature. These results indicate that the reducibility of the samples is enhanced with a low cerium doping which might be related from the formation of more surface oxygen vacancies [9,15,18,43–45].

Fig. 8. H_2-TPR traces of the fresh acid-treated samples

With the addition and increasing content of cerium, the hydrogen consumption decreases per gram of catalyst from 9.20 to 7.53 $mmol/g_{cat}$ while it reaches a maximum value of 0.96 for $Ce_{0.01}Mn$ when expressed as total metal amount (Table 1).

Besides oxygen vacancies, surface acidity is also an important factor that should be taken into consideration for ozone decomposition. The changes of surface acidity induced by the acid treatment have been assessed by adsorption of pyridine on selected samples monitored by FTIR spectroscopy. FTIR analysis of pyridine adsorption allows to determine the balance between Brønsted acid sites (B sites) and Lewis acid sites (L sites). The pyridine FTIR spectra recorded at 105 °C have been exhibited in Fig. 9 for the doped samples $Ce_{0.1}Mn$ and $Ce_{0.2}Mn$ before and after acid treatment. In accordance with the literature [14,46–49], the band assignments have been carried out as follows: bands at 1635 and 1540 cm^{-1} have been attributed to pyridine adsorbed on Brønsted acid sites and bands at 1610 and 1445 cm^{-1} have

been attributed to pyridinium derived from chemisorbed pyridine on L-sites. The band at 1490 cm^{-1} is assigned to pyridine adsorbed on both L-sites and B-sites. The two remaining bands at 1573 cm^{-1} and 1471 cm^{-1} have been ascribed to pyridine physisorption (P) [44,49]. B acid sites can originate from acidic hydroxyl groups attached to metal atoms (Mn, Ce) while L acid sites are regarded as empty orbitals of metal ions in the oxides ($Mn^{4+/3+}$; $Ce^{4+/3+}$). From Fig. 9, it can be shown that no acidity can be detected on the pristine samples. By opposition, L and B sites can be observed on the acid treated samples. The L sites dominated over the B sites when cerium content increases in the sample. As discussed previously, a low doping amount of Ce enhances the surface area throughout an increase of the number of defects and especially of the number of oxygen vacancies. However, some oxygen vacancies may be occupied by water or its dissociative species like hydroxyl groups, which act as Brønsted acid sites.

Fig. 9. Pyridine-FTIR spectra before and after acid treatment for (a) $Ce_{0.01}Mn$ and (b) $Ce_{0.2}Mn$ samples

In order to investigate the effect of acid treatment on the hydrophobicity of the acid-treated samples the amount of adsorbed water per BET specific surface area has been determined from TGA measurements (Table 2) and has been compared to those obtained on the fresh non-treated catalysts as seen in Fig. 10.

Table 2
Water loss between 25 °C and 100 °C determined from TGA measurements expressed in mg/g_{cat}.

Fig. 10. Amount of adsorbed water normalized to the specific surface area

Based on the results, it is shown that the acid-treated catalysts are more hydrophobic than the non-treated counterparts in agreement with previous results [15].

Fig. 11 shows the XPS core level spectra of K 2p (a), O 1s (b), Mn $2p_{3/2}$ (c) and Mn 3s (d) of the acid-treated samples and the salient XPS results are given in Table 3. The intensity of the K 2p signals is very weak, all the more than cerium content is high, in accordance with the ICP-OES results (Table 1). It has to be mentioned that no contribution of Na 1s is observed showing the efficient role of acid treatment to remove Na^+ impurity. The O 1s XPS spectra can be decomposed into three components located at ~ 529.7 eV, ~ 531.3 eV and ~ 533.4 eV which can be attributed to surface lattice oxygen (O_I), oxygen adspecies (O_{II}) and adsorbed H_2O (O_{III}), respectively [50]. Taken into account the decomposition results of Mn $2p_{3/2}$ and O 1s spectra, the Mn^{3+}/Mn^{4+} ratio and the surface adsorbed oxygen concentration ($O_{II}/(O_I + O_{II})$) have been calculated and listed in Table 3. It has to be noted that the possible presence of carbonates on the surface precludes a direct correlation between these two ratios. However the high simultaneous Mn^{3+}/Mn^{4+} ratios whose values increase with Ce content and high adsorbed oxygen concentration are in line with high content of oxygen vacancies [14,18,46,50–53].

Considering both the values of Mn^{3+}/Mn^{4+} ratios and those of the Ce/Mn ICP ratio the highest density of oxygen vacancies can be expected on the $Ce_{0.01}$Mn-AT and $Ce_{0.1}$Mn-AT samples based on charge balance process. It has also to be mentioned that the direct comparison of the Mn^{3+}/Mn^{4+} ratio determined from the Mn $2p_{3/2}$ core level to the Mn AOS determined from the Mn 3s splitting indicates that the extent of reduction is more pronounced in the first layers of the samples. Except $Ce_{0.5}$Mn-AT which exhibits a high enrichment in cerium, the Ce/Mn ratios ranging from 0.008 to 0.097 are consistent with those determined from ICP-OES results.

Fig. 11. XPS spectra of the fresh acid treated samples

Table 3

XPS results of the fresh acid-treated samples

Static ToF-SIMS has also been performed in order to extract surface molecular information and the results are reported in Table 4. In any case, the mixed oxide formation can be easily evidenced by ToF-SIMS through the detection of mixed oxide fragments $Ce_xMn_yO_zH_w^{+/-}$. The enhancement of the $CeMnOH^+/CeOMn^+$ secondary ion ratio after acid treatment suggests an increase of the Brønsted acidity in line with the results of acidic surface site probing by pyridine. Furthermore, comparison of the $MnOH^+/MnO^+$ secondary ion ratio and $CeOH^+/CeO^+$ ratio suggests that Mn is more affected than Ce in surface OH related species.

Table 4
ToF-SIMS results of the fresh acid treated samples

3.4. Characterization studies after O_3 testing

X-ray photoelectron spectroscopy has been used to evidence adsorbed nitrogen related products on the acid-treated Ce_xMn catalyst surfaces. The high-resolution spectra of the N 1s region shown in Fig. 12 highlight the presence of adsorbed nitrogen containing species that differ in the oxidation state of nitrogen atom and the pertinent data have been given in Table 5. Considering the tested acid-treated acid catalysts (Ce_xMn-AT-O_3) a predominant peak at BE of ~ 406.8 eV (N(3)) and small contributions at ~ 403.2 eV (N(2)) and about 399.7 eV (N(3)) have been assigned to adsorbed nitrate (NO_3^-) [54], nitrite (NO_2^-) [54] and to reduced N such as NO^- [55], respectively.

Formation of adsorbed nitrate is observed upon uptake of gaseous HNO_3 and N_2O_5. The formation of NO_3^- (ads) species can occur owing to:

$HNO_3\,(g) = NO_3^-\,(ads) + H^+\,(ads)$

Nitrate can react with Mn/Ce cationic site and the proton on oxygen sites [56,57]. Formation of adsorbed nitrate ions has been previously observed after exposure of hematite (α-Fe_2O_3) surface to gaseous HNO_3 [54]. Regarding N_2O_5, it can autoionize to NO_2^+ and NO_3^- and reacts with water owing to:

$NO_2^+ + NO_3^- + H_2O = 2\ HNO_3$ [58].

The presence of NO_2^- and NO^- are believed to occur from the partial reduction of nitrate into nitrite on the catalysts.

Fig. 12. X-ray photoelectron spectra of the N 1s core level of (a) $Ce_{0.01}Mn$ and (b) $Ce_{0.1}Mn$ at different stages (before and after acid treatment, after test in nearly dry and moist air)

However, it has to be mentioned that a significant contribution of N 1s at about 400.0 eV is always detected for the fresh acid treated catalysts (Ce_xMn-AT) indicating the presence of reduced nitrogen species induced by the acid treatment. Taking this N 1s contribution into account, a corrected N/Mn atomic ratio $(N/Mn)_c$, which is the difference between the N/Mn atomic ratios of the tested and fresh catalysts, has been calculated. It has a value of 0.09 for Mn-B-AT and for the cerium-based catalysts it increases from 0.04 to 0.25 with increasing Ce content. Besides, it is remarkable to note that this ratio correlates with O_3 conversion in agreement with a poisoning of the catalytic sites. Besides, in the presence of significant amount of water (RH = 30 %), $(N/Mn)_c$ drops strongly from 0.04 and 0.09 to 0.01 and 0.02 for $Ce_{0.01}M$-O_3-H and $Ce_{0.1}Mn$-O_3-H, respectively. This decrease is accompanied by a lowering of the nitrate contribution for $Ce_{0.01}M$-O_3-H30 on contrary to $Ce_{0.1}M$-O_3-H30. Additionally, the N(2) contribution located at 403. 0 eV shifts to 401.0 eV and 402.3 eV for Ce/Mn of 0.01 and 0.1, respectively, as seen in Fig. 12a and 12b. Consequently, it is observed a beneficial role of water leading to a decrease of the amount of nitrogen adsorbed species coupled with an increase of reduced surface-bound nitrogen species.

Table 5
N 1s components and N/Mn XPS ratios for the tested catalysts

FTIR-ATR has also been used for detecting surface nitrogen containing species after testing in nearly dry and moist air at 30 °C and 40 °C for the best catalyst $Ce_{0.01}Mn$-AT. Tentative band assignments of FTIR-ATR spectra have been done based on XPS results showing that most nitrogen containing species on Ce_xMn catalysts are nitrates (not shown here). In addition to free nitrate ion, NO_3^- can be coordinated in different ways (monodentate, bidentate chelating and/or bridging) [56]. The FTIR-ATR spectra recorded between 700 cm^{-1} and 1820 cm^{-1} are displayed in Fig. 13a along with reference FTIR-ATR spectrum of potassium nitrate (Fig. 13b).

Fig. 13. FTIR-ATR spectra of (a) tested $Ce_{0.01}Mn$-AT catalysts (b) reference metal alkali nitrates; (c) $Ce_{0.01}Mn$-AT-O_3-H30 before and after heating at 200 °C for 4 h.

Considering the FTIR-ATR spectrum of $Ce_{0.1}Mn$-AT-O_3 the band which appears at the highest frequency positioned at 1617 cm^{-1} has been assigned to the bending mode of water [49]. The two distinct bands in the medium frequency range (1400-1200 cm^{-1}) at 1384 and 1316 cm^{-1} have been attributed by comparison with the reference spectrum of potassium nitrate (Fig. 13b) and nitrite [59] assigned to adsorbed ionic nitrate (Fig. 13b) and nitrite [59] in interaction with K^+, respectively. In moist air (RH = 30 %) the number of bands increases all the more that the temperature of the catalytic reactor decreases. At 30°C, among the new bands which appear, those at about 1500 and 1251 cm^{-1} have been attributed to bidentate NO_3^- [56] linked to manganese cations in accordance with the works of D. Pozdnyakov *et al.* [60]. The effect of temperature on the adsorbed nitrogen containing species has also been investigated in the case of $Ce_{0.01}Mn$-AT-O_3-H30. (Fig. 13c) through the comparison of the FTIR-ATR spectra obtained before and after heating the sample at 200 °C for 4 h in an oven ($Ce_{0.01}Mn$-AT-O_3-H30-200). It is observed that the prominent IR bands at 1390 cm^{-1} and 1323

cm^{-1} decrease strongly in intensity as compared to the other ones. As expected, this indicates clearly that the ionic nitrates and nitrites interact in a less effective manner than the nitrato ligands.

3.5. Effect of nitrogen containing co-pollutants and water for gaseous ozone decomposition

The redox method followed by an acidic treatment allow to get materials with a high specific surface area around 300 m^2/g (Table 1) with good redox properties. When adding small amounts of cerium, the oxygen mobility as well as the acidity are greatly improved. However, for a high Ce/Mn ratio of 0.5 the beneficial effects on the redox properties are no longer observed owing to a decrease of the cerium dispersion. The decrease of the O_3 conversion over time for the undoped acid-treated catalyst is due to a partial poisoning effect due to nitrogen containing compounds. The better performances of the low Ce containing catalysts can be explained by improved redox properties allowing to a decrease of the adsorbed nitrogen containing species.

Additionally, the high activity of Ce_xMn-AT (x = 0.01;0.1) in moist air (RH = 30 %) in the presence of nitrogen containing co-pollutants can be envisioned considering the mechanism for O_3 decomposition in humid air involving acid sites and oxygen vacancies proposed by Liu *et al.* [15]. More water acid sites in interaction with oxygen vacancy allows a better hydrophobic catalyst which can facilitate the adsorption and subsequent decomposition of gaseous ozone. Furthermore, in the presence of water the contribution of nitrogen adspecies is significantly lowered and the distribution of reduced nitrogen based adspecies is much more important suggesting catalyst reduction of NO_3^- adsorbed species.

5. Conclusion

A pioneer series of experiments were performed to study the decomposition of ozone in the presence of nitrogen pollutants and humidity on acid-treated Ce modified birnessites. The main findings could be summarized as follows: The performances of ozone decomposition were closely related to the presence of nitrogen pollutants. At very low humidity, the acid treated catalysts showed a minimization of deactivation. At higher RH, after an induction period, the acid treated catalysts were effective for the elimination of ozone and stable during 5 h of reaction. Higher amounts of oxygen vacancies and acid sites were invoked to improve water resistance properties and to decrease nitrate interaction. The generation of such efficient catalysts open new perspectives for ozone decomposition from polluted air.

Acknowledgments:

This research is supported by a European Program INTERREG V France-Wallonie-Flanders (FEDER) (DepollutAir). Chevreul institute (FR 2638), Ministère de l'Enseignement Supérieur et de la Recherche and Région Hauts-de-France are acknowledged for supporting this work. This research was carried out in the French-Belgium Associated International Laboratory "Plasma & Catalysis" supported by the universities of Lille and Ghent. The authors thank Nicolas Nuns, Christine Lancelot, Pardis Simon, Laurence Burylo, Olivier Gardoll and Jean-Charles Morin for their contribution in ToF-SIMS, TEM, XPS, XRD, TPD and IR-pyridine measurements, respectively.

References:

[1] M. Shao, Y. Zhang, L. Zeng, X. Tang, J. Zhang, L. Zhong, B. Wang, Ground-level ozone in the Pearl River Delta and the roles of VOC and NO_x in its production, J. of Environ. Manage. 90 (2009) 512–518. https://doi.org/10.1016/j.jenvman.2007.12.008.

[2] P. Wolkoff, Indoor air pollutants in office environments: Assessment of comfort, health, and performance, Int. J. Hyg. Envir. Heal. 216 (2013) 371–394. https://doi.org/10.1016/j.ijheh.2012.08.001.

[3] Daniel Vallebero, Fundamentals of Air Pollution, Fifth edition, chapter 7 Air pollutant hazards (2014) 197-214.

[4] C.-C. Lin, C.-Y. Chao, M.-Y. Liu, Removal of ozone from air by absorption in a rotating packed bed, J. Ind. Eng. Chem. 16 (2010) 140–146. https://doi.org/10.1016/j.jiec.2010.01.005.

[5] X. Luo, T. Su, X. Xie, Z. Qin, H. Ji, The Adsorption of Ozone on the Solid Catalyst Surface and the Catalytic Reaction Mechanism for Organic Components, ChemistrySelect. 5 (2020) 15092–15116. https://doi.org/10.1002/slct.202003805.

[6] T. Batakliev, V. Georgiev, M. Anachkov, S. Rakovsky, S. Rakovsky, Ozone decomposition, Interdiscip. Toxicolo. 7 (2014) 47–59. https://doi.org/10.2478/intox-2014-0008

[7] B. Dhandapani, S.T. Oyama, Gas phase ozone decomposition catalysts, Appl.Catal. B: Environ. 11 (1997) 129–166. https://doi.org/10.1016/S0926-3373(96)00044-6

[8] S. Imamura, M. Ikebata, T. Ito, T. Ogita, Decomposition of ozone on a silver catalyst, Ind. Eng. Chem. Res. 30 (1991) 217–221. https://doi.org/10.1021/ie00049a033.

[9] J.Jia, P. Zhang, L. Chen, C. Catalytic decomposition of gaseous ozone over manganese dioxides with different crystal structures, Appl. Catal. B: Environ. 189 (2016) 210-218. https://doi.org/ 10.1016/j.apcatb.2016.02.055

[10] T. Gopi, G. Swetha, S. Chandra Shekar, C. Ramakrishna, B. Saini, R. Krishna, P.V.L. Rao, Catalytic decomposition of ozone on nanostructured potassium and proton containing δ-MnO_2 catalysts, Catal. Commun. 92 (2017) 51–55. https://doi.org/10.1016/j.catcom.2017.01.002.

[11] G. Zhu, J. Zhu, W. Jiang, Z. Zhang, J. Wang, Y. Zhu, Q. Zhang, Surface oxygen vacancy induced α-MnO_2 nanofiber for highly efficient ozone elimination, Appl. Catal. B: Environ. 209 (2017) 729–737. https://doi.org/10.1016/j.apcatb.2017.02.068.

[12] H. Deng, S. Kang, J. Ma, L. Wang, C. Zhang, H. He, Role of Structural Defects in MnO_x Promoted by Ag Doping in the Catalytic Combustion of Volatile Organic Compounds and Ambient Decomposition of O_3, Environ. Sci. Technol. 53 (2019) 10871–10879. https://doi.org/10.1021/acs.est.9b01822

[13] X. Li, J. Ma, C. Zhang, R. Zhang, H. He, Detrimental role of residual surface acid ions on ozone decomposition over Ce-modified γ-MnO_2 under humid conditions, J. Environ. Sci. 91 (2020) 43–53. https://doi.org/10.1016/j.jes.2019.12.004.

[14] Y. Liu, H. Zhou, R. Cao, X. Liu, P. Zhang, J. Zhan, L. Liu, Facile and green synthetic strategy of birnessite-type MnO_2 with high efficiency for airborne benzene removal at low temperatures, Appl. Catal. B: Environ. 245 (2019) 569–582. https://doi.org/10.1016/j.apcatb.2019.01.023

[15] Y. Liu, W. Yang, P. Zhang, J. Zhang, Nitric acid-treated birnessite-type MnO 2 : An efficient and hydrophobic material for humid ozone decomposition, Appl. Surf. Sci. 442 (2018) 640–649. https://doi.org/10.1016/j.apsusc.2018.02.204.

[16] Y. Wang, F. Wang, Q. Song, Q. Xin, S. Xu, J. Xu, Heterogeneous Ceria Catalyst with Water-Tolerant Lewis Acidic Sites for One-Pot Synthesis of 1,3-Diols via Prins

Condensation and Hydrolysis Reactions, J. Am. Chem. Soc. 135 (2013) 1506–1515. https://doi.org/10.1021/ja310498c.
[17] Z. Lian, J. Ma, H. He, Decomposition of high-level ozone under high humidity over Mn-Fe catalyst: The influence of iron precursors, Catal. Commun. 59 (2015) 156–160. https://doi.org/10.1016/j.catcom.2014.10.005.
[18] L. Zhu, J. Wang, S. Rong, H. Wang, P. Zhang, Cerium modified birnessite-type MnO_2 for gaseous formaldehyde oxidation at low temperature, Appl. Catal. B: Environ. 211 (2017) 212–221. https://doi.org/10.1016/j.apcatb.2017.04.025.
[19] Y. Liu, P. Zhang, Catalytic decomposition of gaseous ozone over todorokite-type manganese dioxides at room temperature: Effects of cerium modification, Appl. Catal. A: Gen. 530 (2017) 102–110. https://doi.org/10.1016/j.apcata.2016.11.028.
[20] R. Sindhu, G. Amba Prasad Rao, K. Madhu Murthy, Effective reduction of NO_x emissions from diesel engine using split injections, Alex. Eng. J. 57 (2018) 1379–1392. https://doi.org/10.1016/j.aej.2017.06.009.
[21] H. Touati, A. Guerin, Y. Swesi, C.B. Dupeyrat, R. Philippe, V. Meille, J.-M. Clacens, Unexpected role of NO_x during catalytic ozone abatement at low temperature, Catal. Commun. 148 (2021) 106163. https://doi.org/10.1016/j.catcom.2020.106163.
[22] B.S. Patil, N. Cherkasov, J. Lang, A.O. Ibhadon, V. Hessel, Q. Wang, Low temperature plasma-catalytic NOx synthesis in a packed DBD reactor: Effect of support materials and supported active metal oxides, App. Catal. B: Environ. 194 (2016) 123–133. https://doi.org/10.1016/j.apcatb.2016.04.055.
[23] N. Cherkasov, A.O. Ibhadon, P. Fitzpatrick, A review of the existing and alternative methods for greener nitrogen fixation, Chem. Eng. Process. 90 (2015) 24–33. https://doi.org/ 10.1016/j.cep.2015.02.004.
[24] Y. Qin, S. Qian, C. Wang, W. Xia, Effects of nitrogen on ozone synthesis in packed-bed dielectric barrier discharge, Plasma Sci. Technol., 20 (2018) 095501. https://doi.org/ 10.1088/2058-6272/aac203.
[25] D. Mehandjiev, A. Naydenov, G. Ivanov, Ozone decomposition, benzene and CO oxidation over $NiMnO_3$-ilmenite and $NiMn_2O_4$-spinel catalysts, Appl. Catal. A: Gen. 206 (2001) 13–18. https://doi.org/10.1016/S0926-860X(00)00570-6.
[26] C. Subrahmanyam, D.A. Bulushev, L. Kiwi-Minsker, Dynamic behaviour of activated carbon catalysts during ozone decomposition at room temperature, Appl. Catal. B: Environ. 61 (2005) 98–106. https://doi.org/10.1016/j.apcatb.2005.04.013.
[27] M. Händel, T. Rennert, K.U. Totsche, A simple method to synthesize birnessite at ambient pressure and temperature, Geoderma, 193–194 (2013) 117–121. https://doi.org/10.1016/j.geoderma.2012.09.002.
[28] M.C. Biesinger, B.P. Payne, A.P. Grosvenor, L.W.M. Lau, A.R. Gerson, R.St.C. Smart, Resolving surface chemical states in XPS analysis of first row transition metals, oxides and hydroxides: Cr, Mn, Fe, Co and Ni, Appl. Surf. Sci. 257 (2011) 2717–2730. https://doi.org/10.1016/j.apsusc.2010.10.051.
[29] L. Zhang, J. Tu, L. Lyu, C. Hu, Enhanced catalytic degradation of ciprofloxacin over Ce-doped OMS-2 microspheres, Appl. Catal. B: Environ. 181 (2016) 561–569. https://doi.org/10.1016/j.apcatb.2015.08.029.
[30] V.R. Galakhov, M. Demeter, S. Bartkowski, M. Neumann, N.A. Ovechkina, E.Z. Kurmaev, N.I. Lobachevskaya, Ya.M. Mukovskii, J. Mitchell, D.L. Ederer, Mn3s exchange splitting in mixed-valence manganites, Phys. Rev. B, 65 (2002) 113102. https://doi.org/10.1103/PhysRevB.65.113102.
[31] V.P. Santos, M.F.R. Pereira, J.J.M. Órfão, J.L. Figueiredo, Catalytic oxidation of ethyl acetate over a cesium modified cryptomelane catalyst, Appl. Catal. B: Environ. 88 (2009) 550–556. https://doi.org/10.1016/j.apcatb.2008.10.006.

[32] J. Wang, R. Yunus, J. Li, P. Li, P. Zhang, J. Kim, In situ synthesis of manganese oxides on polyester fiber for formaldehyde decomposition at room temperature, Appl. Surf. Sci. 357 (2015) 787–794. https://doi.org/10.1016/j.apsusc.2015.09.109.
[33] S. Sultana, Z. Ye, S.K.P. Veerapandian, A. Löfberg, N. De Geyter, R. Morent, J.M. Giraudon, J.F. Lamonier, Synthesis and catalytic performances of K-OMS-2, Fe/K-OMS-2 and Fe-K-OMS-2 in post plasma-catalysis for dilute TCE abatement, Catal. Today, (2016) 0–1. https://doi.org/10.1016/j.cattod.2017.05.078.
[34] Yu.S. Akishev, G.I. Aponin, V.B. Karal'nik, a. E. Monich, N.I. Trushkin, Phenomenology of a high-current negative point-to-plane corona in nitrogen, Plasma Phys. Rep. 30 (2004) 779–787. https://doi.org/10.1134/1.1800224.
[35] C. Sun, N. Zhao, Z. Zhuang, H. Wang, Y. Liu, X. Weng, Z. Wu, Mechanisms and reaction pathways for simultaneous oxidation of NO_x and SO_2 by ozone determined by in situ IR measurements, J. Hazard. Mater. 274 (2014) 376–383. https://doi.org/10.1016/j.jhazmat.2014.04.027.
[36] V.A. Drits, E. Silvester, A.I. Gorshkov, A. Manceau, Structure of synthetic monoclinic Na-rich birnessite and hexagonal birnessite; I, Results from X-ray diffraction and selected-area electron diffraction, Am. Min. 82 (1997) 946–961. https://doi.org/10.2138/am-1997-9-1012.
[37] S. Royer, D. Duprez, S. Kaliaguine, Role of bulk and grain boundary oxygen mobility in the catalytic oxidation activity of $LaCo_{1-x}Fe_xO_3$, J. Catal. 234 (2005) 364–375. https://doi.org/10.1016/j.jcat.2004.11.041.
[38] R. Vidruk, M.V. Landau, M. Herskowitz, M. Talianker, N. Frage, V. Ezersky, N. Froumin, Grain boundary control in nanocrystalline MgO as a novel means for significantly enhancing surface basicity and catalytic activity, J. Catal. 263 (2009) 196–204. https://doi.org/10.1016/j.jcat.2009.02.014.
[39] H. Hojo, T. Mizoguchi, H. Ohta, S.D. Findlay, N. Shibata, T. Yamamoto, Y. Ikuhara, Atomic Structure of a CeO_2 Grain Boundary: The Role of Oxygen Vacancies, Nano. Lett. 10 (2010) 4668–4672. https://doi.org/10.1021/nl1029336.
[40] Q. Fu, W.-X. Li, Y. Yao, H. Liu, H.-Y. Su, D. Ma, X.-K. Gu, L. Chen, Z. Wang, H. Zhang, B. Wang, X. Bao, Interface-Confined Ferrous Centers for Catalytic Oxidation, Science, 328 (2010) 1141–1144. https://doi.org/10.1126/science.1188267.
[41] M. Sakai, Y. Nagai, Y. Aoki, N. Takahashi, Investigation into the catalytic reduction of NO at copper–ceria interface active sites, Appl. Catal. A: Gen. 510 (2016) 57–63. https://doi.org/10.1016/j.apcata.2015.11.007.
[42] W. Gac, G. Słowik, W. Zawadzki, Structural and surface changes of copper modified manganese oxides, Appl. Surf. Sci. 370 (2016) 536–544. https://doi.org/10.1016/j.apsusc.2016.02.136.
[43] B.-B. Chen, X.-B. Zhu, Y.-D. Wang, L.-M. Yu, J.-Q. Lu, C. Shi, Nano-sized gold particles dispersed on HZSM-5 and SiO_2 substrates for catalytic oxidation of HCHO, Catal. Today, 281 (2017) 512–519. https://doi.org/10.1016/j.cattod.2016.06.023.
[44] J. Chen, X. Chen, D. Yan, M. Jiang, W. Xu, H. Yu, H. Jia, A facile strategy of enhancing interaction between cerium and manganese oxides for catalytic removal of gaseous organic contaminants, Appl. Catal. B: Environ. 250 (2019) 396–407. https://doi.org/10.1016/j.apcatb.2019.03.042.
[45] P. Zhang, H. Lu, Y. Zhou, L. Zhang, Z. Wu, S. Yang, H. Shi, Q. Zhu, Y. Chen, S. Dai, Mesoporous MnCeOx solid solutions for low temperature and selective oxidation of hydrocarbons, Nat Commun, 6 (2015) 8446. https://doi.org/10.1038/ncomms9446.
[46] Y. Liu, W. Yang, P. Zhang, J. Zhang, Nitric acid-treated birnessite-type MnO_2: An efficient and hydrophobic material for humid ozone decomposition, Appl. Surf. Sci. 442 (2018) 640–649. https://doi.org/10.1016/j.apsusc.2018.02.204.

[47] R. Cao, P. Zhang, Y. Liu, X. Zheng, Ammonium-treated birnessite-type MnO_2 to increase oxygen vacancies and surface acidity for stably decomposing ozone in humid condition, Appl. Surf. Sci. 495 (2019) 143607. https://doi.org/10.1016/j.apsusc.2019.143607.
[48] B. de Rivas, R. López-Fonseca, J.R. González-Velasco, J.I. Gutiérrez-Ortiz, On the mechanism of the catalytic destruction of 1,2-dichloroethane over Ce/Zr mixed oxide catalysts, J. Mol. Catal. A: Chem. 278 (2007) 181–188. https://doi.org/10.1016/j.molcata.2007.09.006.
[49] E. Eren, H. Gumus, B. Eren, A. Sarihan, Surface Acidity of H-Birnessite: Infrared Spectroscopic Study of Formic Acid Decomposition, An International Journal for Rapid Communivation 8 (2012) 60-66. https://doi.org/10.1080/00387010.2012.666612
[50] T. Mathew, K. Suzuki, Y. Ikuta, N. Takahashi, H. Shinjoh, Mesoporous ferrihydrite with incorporated manganese for rapid removal of organic contaminants in air, Chem. Commun. 48 (2012) 10987. https://doi.org/10.1039/c2cc36120e.
[51] D.R. Mullins, S.H. Overbury, D.R. Huntley, Electron spectroscopy of single crystal and polycrystalline cerium oxide surfaces, Surf. Sci. 409 (1998) 307–319. https://doi.org/10.1016/S0039-6028(98)00257-X
[52] H. Wang, J. Zhang, X. Hang, X. Zhang, J. Xie, B. Pan, Y. Xie, Half-Metallicity in Single-Layered Manganese Dioxide Nanosheets by Defect Engineering, Angew. Chem. Intern. Ed. Engl. 54 (2015) 1195–1199. https://doi.org/10.1002/anie.201410031.
[53] S. Selvakumar, N. Nuns, M. Trentesaux, V.S. Batra, J.-M. Giraudon, J.-F. Lamonier, Reaction of formaldehyde over birnessite catalyst: A combined XPS and ToF-SIMS study, Appl. Catal. B: Environ. 223 (2018) 192–200. https://doi.org/10.1016/j.apcatb.2017.05.029.
[54] C.E. Nanayakkara, P.M. Jayaweera, G. Rubasinghege, J. Baltrusaitis, V.H. Grassian, Surface Photochemistry of Adsorbed Nitrate: The Role of Adsorbed Water in the Formation of Reduced Nitrogen Species on α-Fe_2O_3 Particle Surfaces, J. Phys. Chem. A. 118 (2014) 158–166. https://doi.org/10.1021/jp409017m.
[55] J. Baltrusaitis, P.M. Jayaweera, V.H. Grassian, XPS study of nitrogen dioxide adsorption on metal oxide particle surfaces under different environmental conditions, Phys. Chem. Chem. Phys. 11 (2009) 8295. https://doi.org/10.1039/b907584d.
[56] K.I. Hadjiivanov, Identification of Neutral and Charged N_xO_y Surface Species by IR Spectroscopy, Catal. Rev. 42 (2000) 71–144. https://doi.org/10.1081/CR-100100260.
[57] M. Machida, M. Uto, D. Kurogi, T. Kijima, MnO_x–CeO_2 Binary Oxides for Catalytic NO_x Sorption at Low Temperatures Sorptive Removal of NO_x, Chem. Mater. 12 (2000) 3158–3164. https://doi.org/10.1021/cm000207r.
[58] L. Brouwer, M.J. Rossi, D.M. Golden, Reaction of N_2O, with H_2O on Carbonaceous Surfaces, J.Phys.Chem. 5 (1986) 4599-4603.
[59] M.H. Brooker, D.E. Irish, Infrared and Raman Spectroscopic Studies of Solid Alkali Metal Nitrites, Can. J. Chem., 49 (1971) 1289–1295. https://doi.org/ 10.1139/v71-210.
[60] D.V. Pozdnyakov, V.N. Filimonov, Infrared study of molecular complexes arising from adsorption of NO and NO_2 on the surface of oxides, Adv. Mol. Relax. Pr. 5 (1973) 55–63. https://doi.org/10.1016/0001-8716(73)80019-7.

Fig. 1.

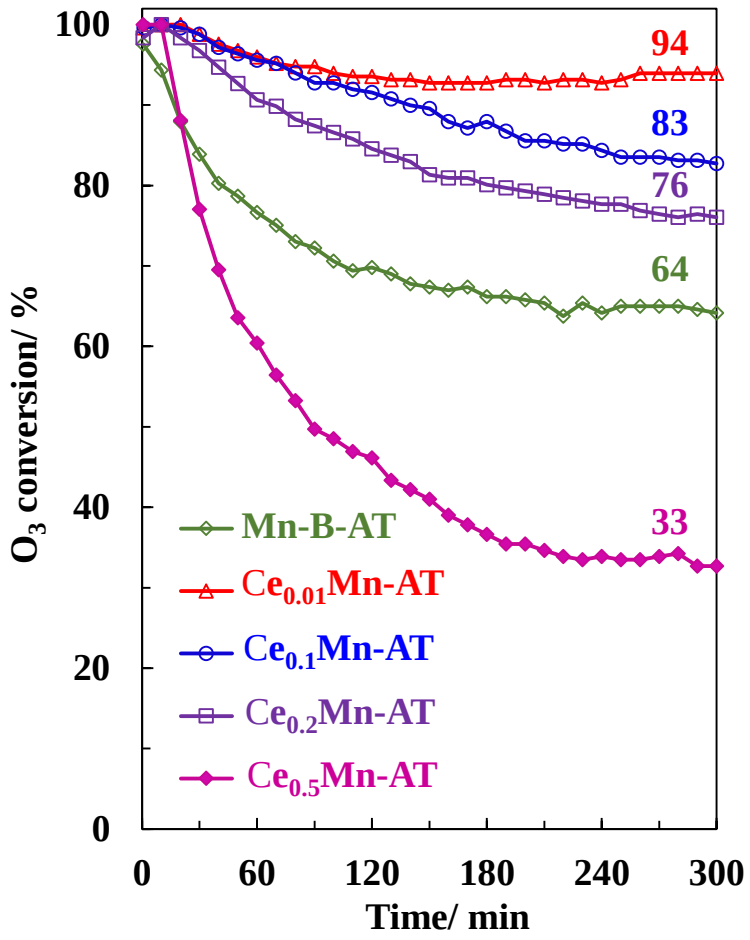
100
80
60
40
20
0
0
60
120
180
240
300
Time/ min
O3 conversion/ %
94
83
76
64
33
Mn-B-AT
Ce0.01Mn-AT
Ce0.1Mn-AT
Ce0.2Mn-AT
Ce0.5Mn-AT

Fig. 2.

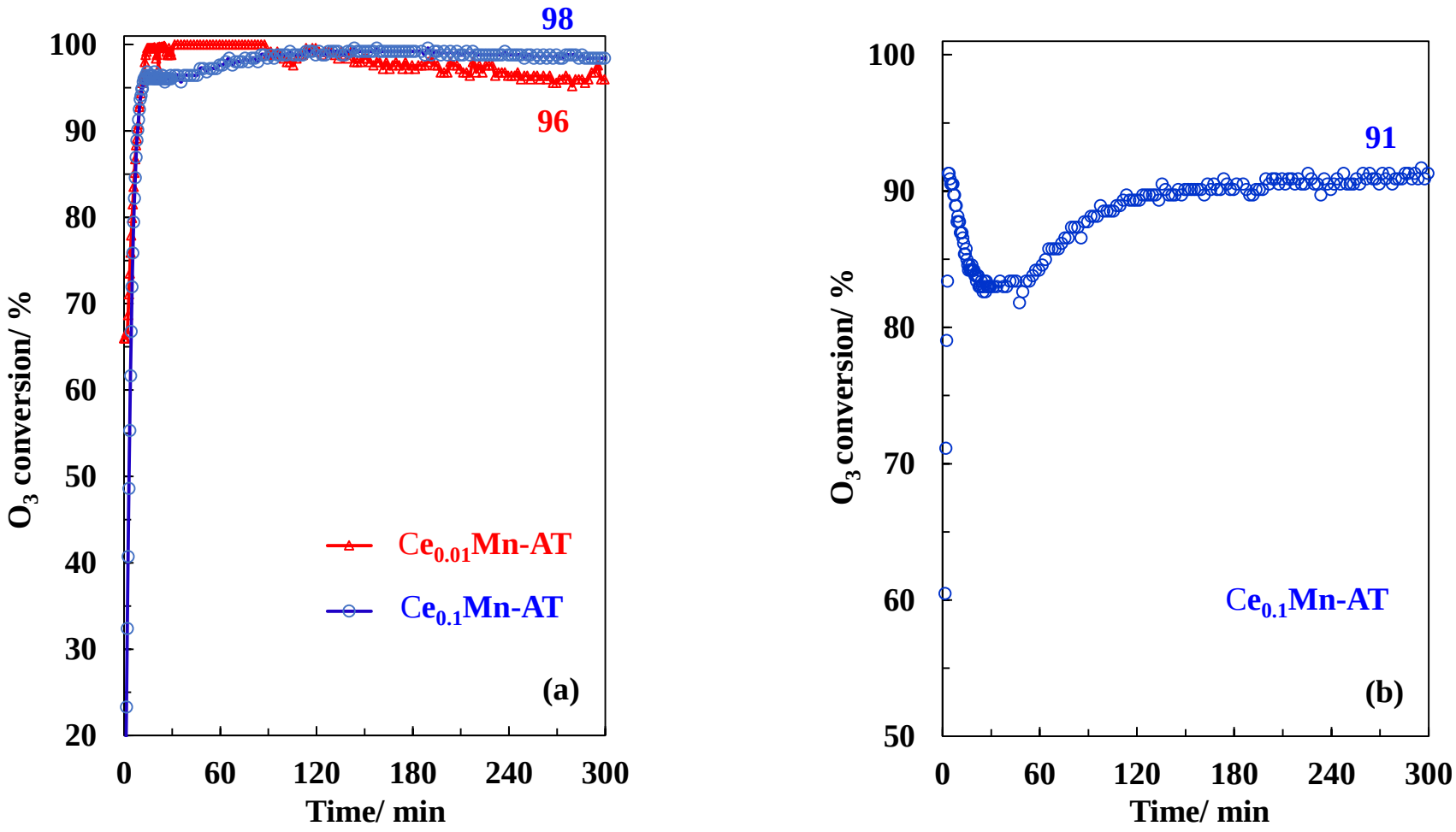
98
96
100
90
80
70
60
50
40
30
20
O_3 conversion/ %
0
60
120
180
240
300
Time/ min
$Ce_{0.01}Mn$-AT
$Ce_{0.1}Mn$-AT
(a)
91
$Ce_{0.1}Mn$-AT
(b)

Fig. 3.

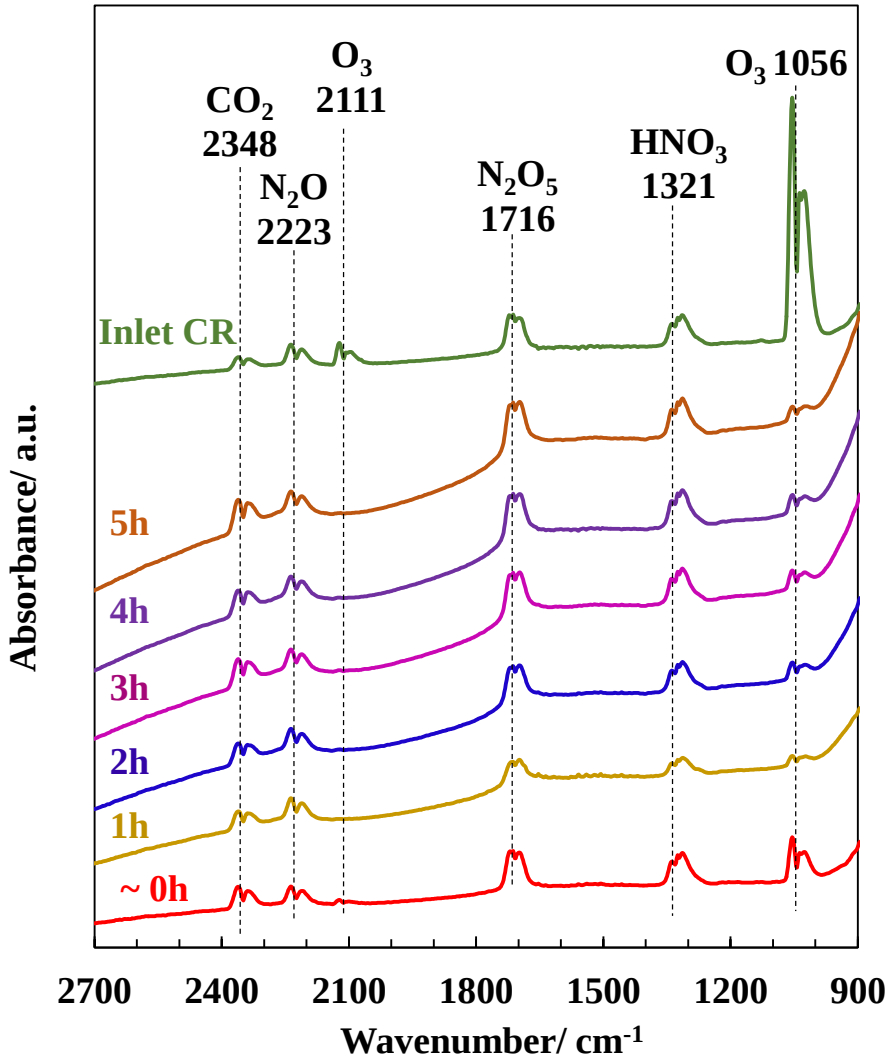
CO_2 2348
O_3 2111
N_2O 2223
N_2O_5 1716
HNO_3 1321
O_3 1056
Inlet CR
5h
4h
3h
2h
1h
~ 0h
Absorbance/ a.u.
2700
2400
2100
1800
1500
1200
900
Wavenumber/ cm^{-1}

Fig. 4.

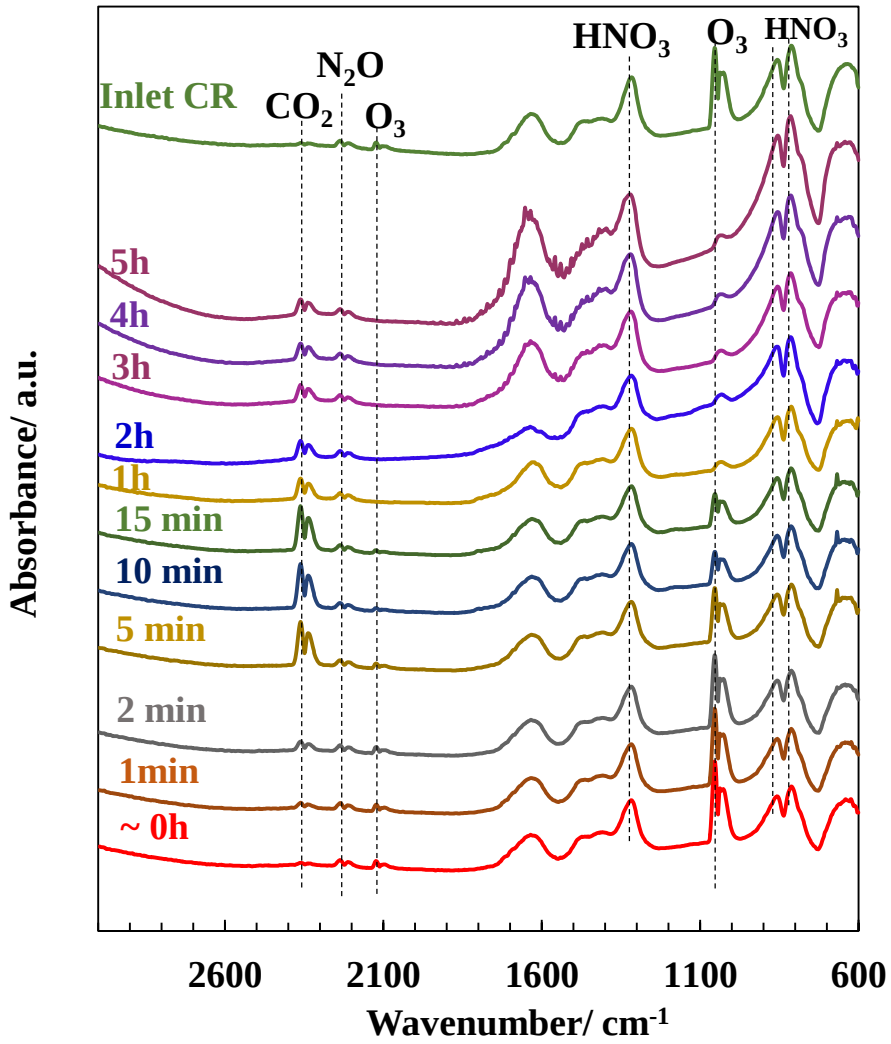
HNO3
O3
HNO3
N2O
CO2
O3
Inlet CR
5h
4h
3h
2h
1h
15 min
10 min
5 min
2 min
1min
~ 0h
Absorbance/ a.u.
2600
2100
1600
1100
600
Wavenumber/ cm-1

Fig. 5.

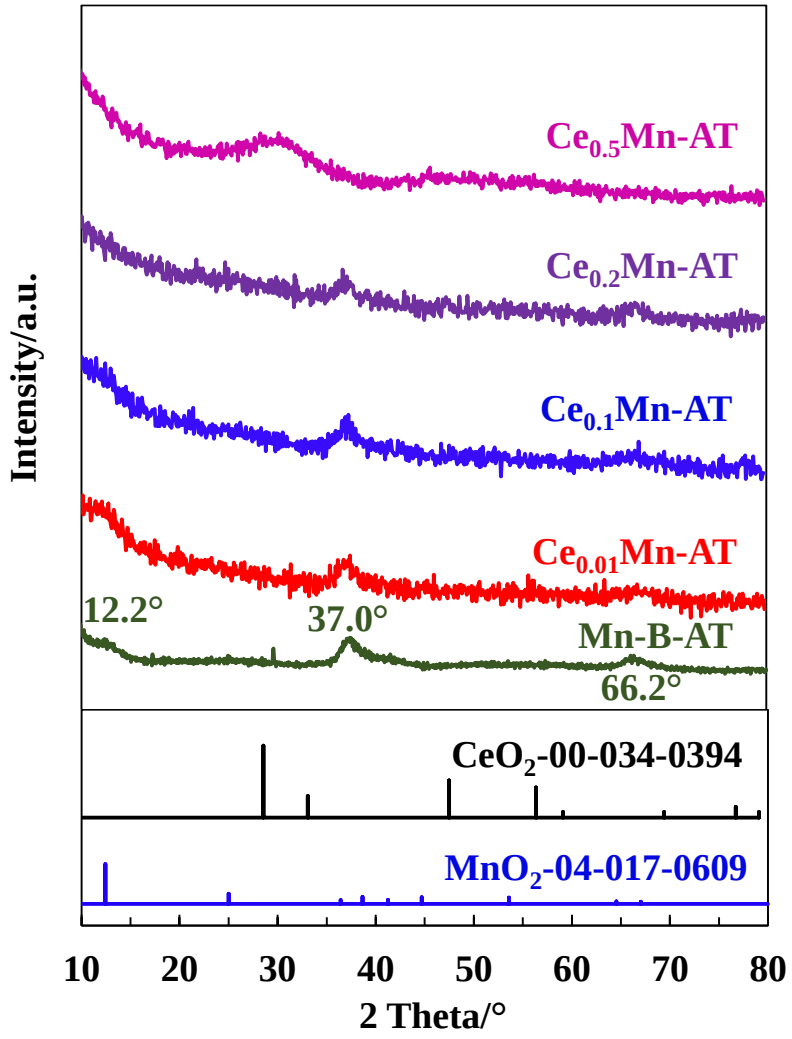
Ce0.5Mn-AT
Ce0.2Mn-AT
Ce0.1Mn-AT
Ce0.01Mn-AT
12.2°
37.0°
Mn-B-AT
66.2°
CeO2-00-034-0394
MnO2-04-017-0609
Intensity/a.u.
10
20
30
40
50
60
70
80
2 Theta/°

Fig. 6.

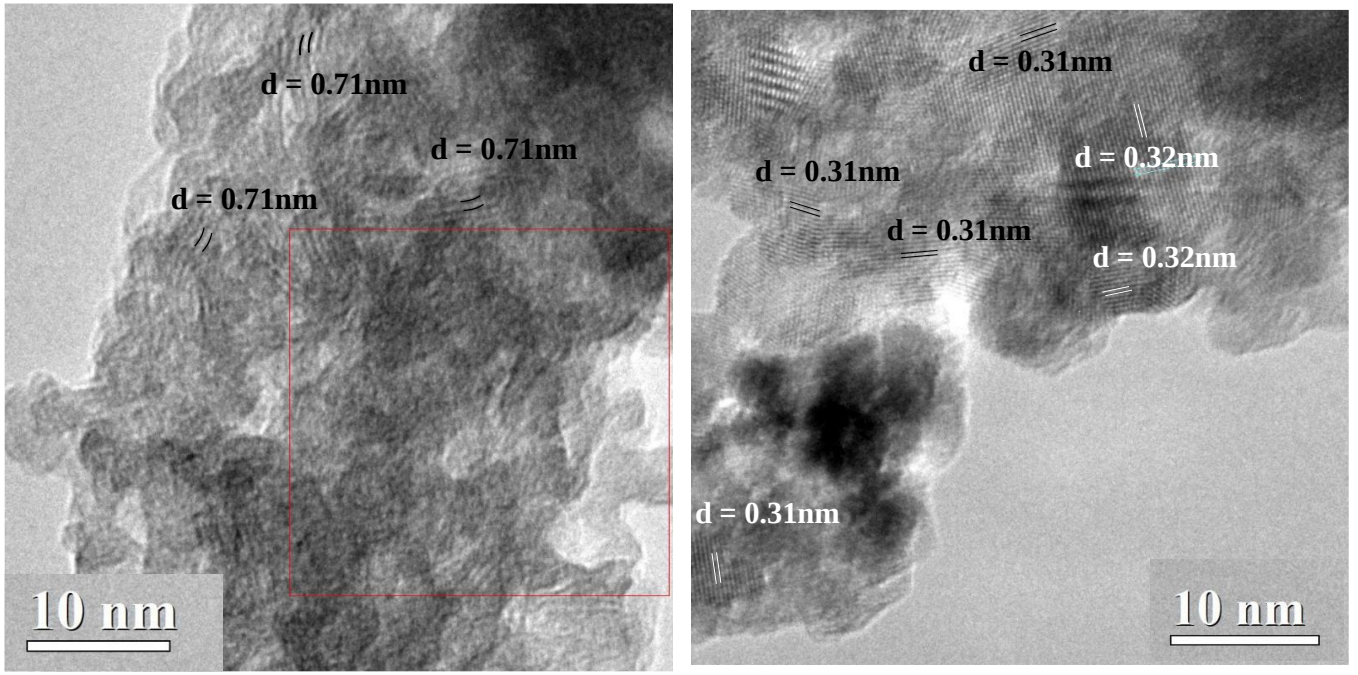
d = 0.71nm
d = 0.71nm
d = 0.71nm
10 nm
d = 0.31nm
d = 0.32nm
d = 0.31nm
d = 0.31nm
d = 0.32nm
d = 0.31nm
10 nm

Fig. 7.

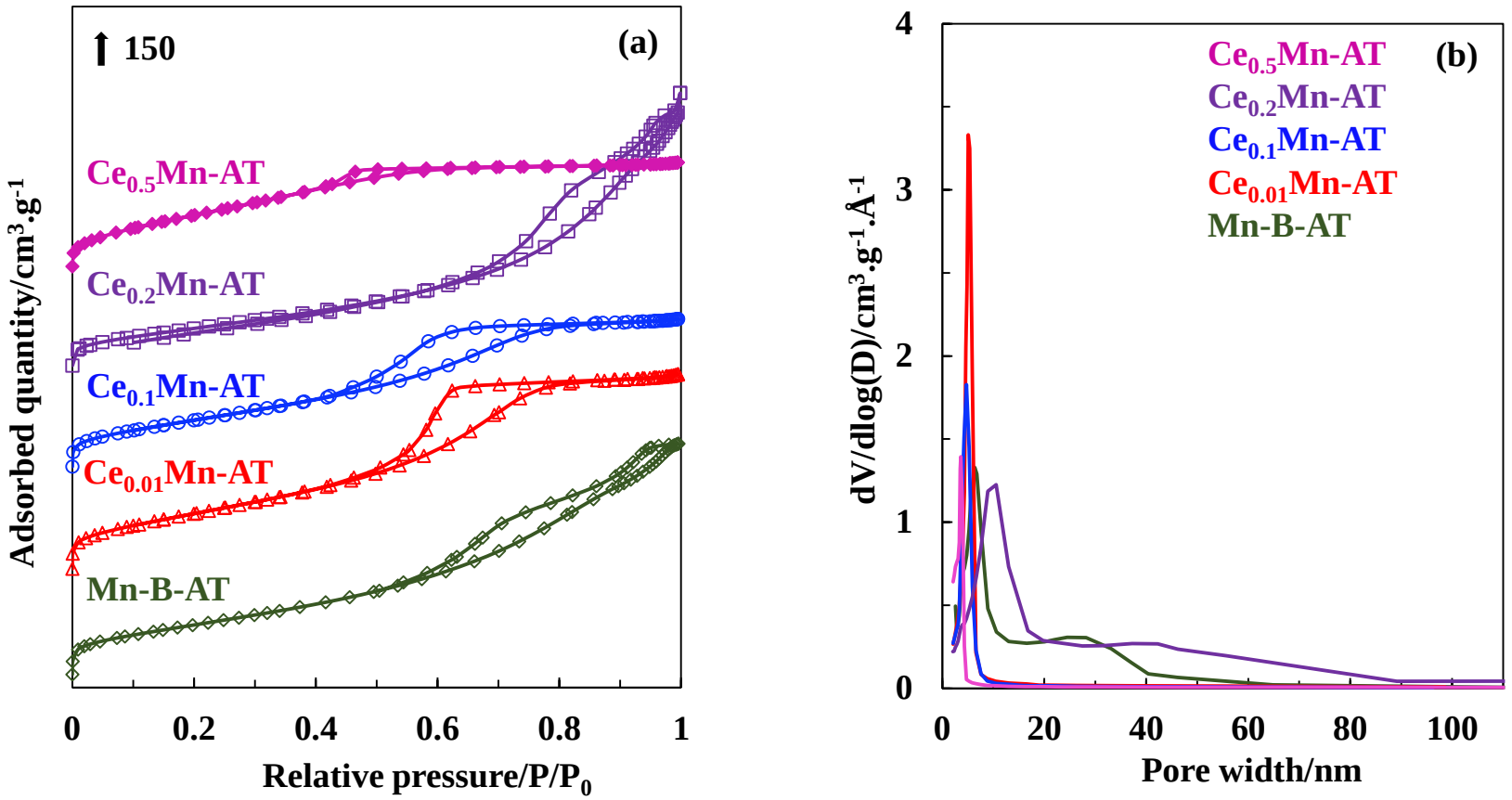
150
(a)
Ce0.5Mn-AT
Ce0.2Mn-AT
Ce0.1Mn-AT
Ce0.01Mn-AT
Mn-B-AT
Adsorbed quantity/cm3.g-1
Relative pressure/P/P0
0
0.2
0.4
0.6
0.8
1
(b)
dV/dlog(D)/cm3.g-1.Å-1
Pore width/nm
0
1
2
3
4
0
20
40
60
80
100

Fig. 8.

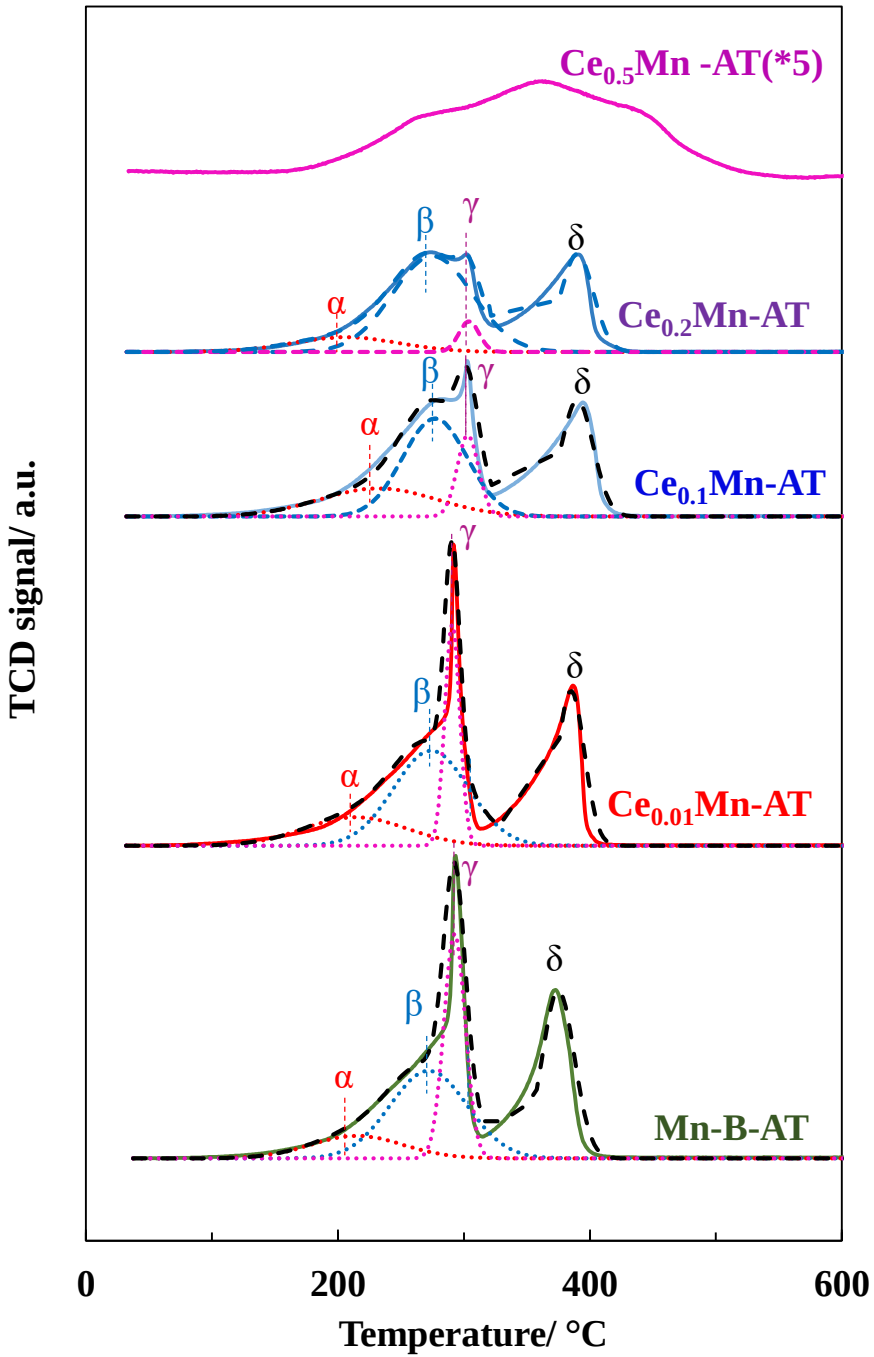
Ce0.5Mn -AT(*5)
β
γ
δ
α
Ce0.2Mn-AT
Ce0.1Mn-AT
Ce0.01Mn-AT
Mn-B-AT
TCD signal/ a.u.
0
200
400
600
Temperature/ °C

Fig. 9.

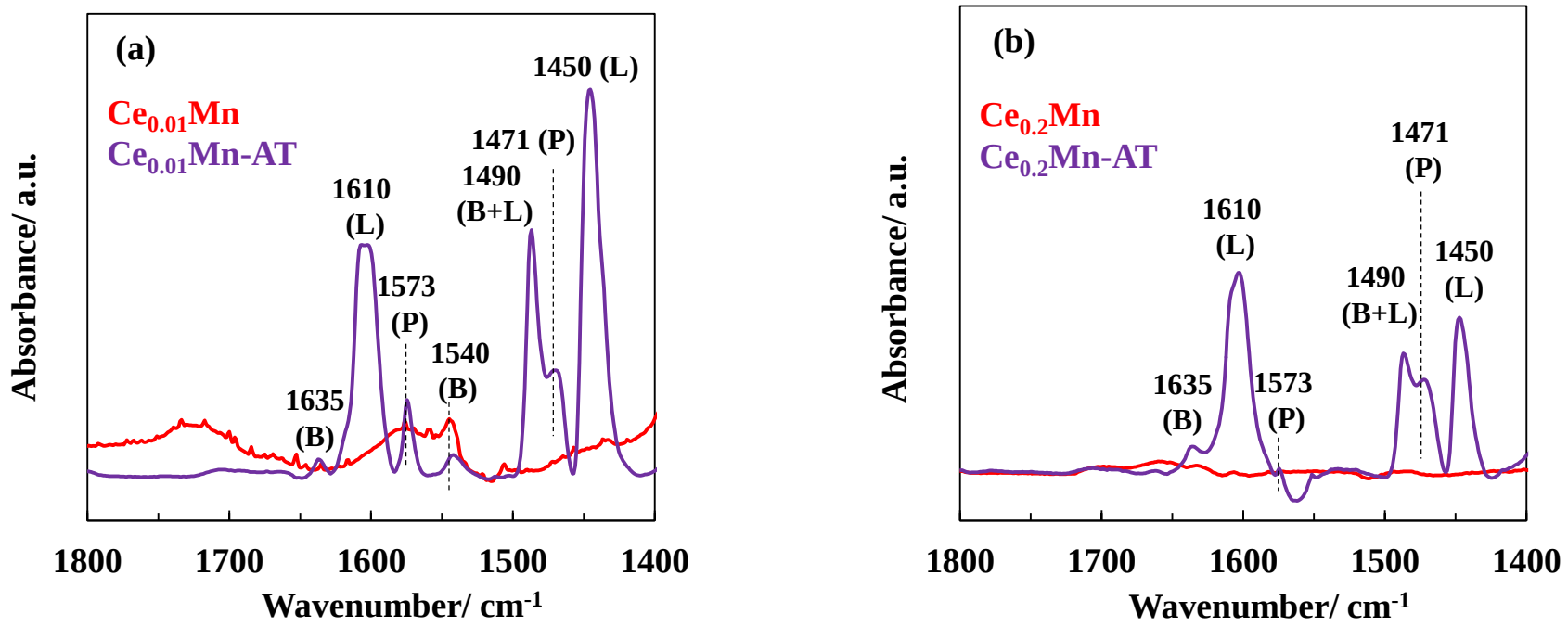
(a)
Ce0.01Mn
Ce0.01Mn-AT
1450 (L)
1471 (P)
1490
(B+L)
1610
(L)
1573
(P)
1540
(B)
1635
(B)
Absorbance/ a.u.
1800
1700
1600
1500
1400
Wavenumber/ cm-1
(b)
Ce0.2Mn
Ce0.2Mn-AT
1471
(P)
1610
(L)
1490
(B+L)
1450
(L)
1635
(B)
1573
(P)
Absorbance/ a.u.
1800
1700
1600
1500
1400
Wavenumber/ cm-1

Fig. 10.

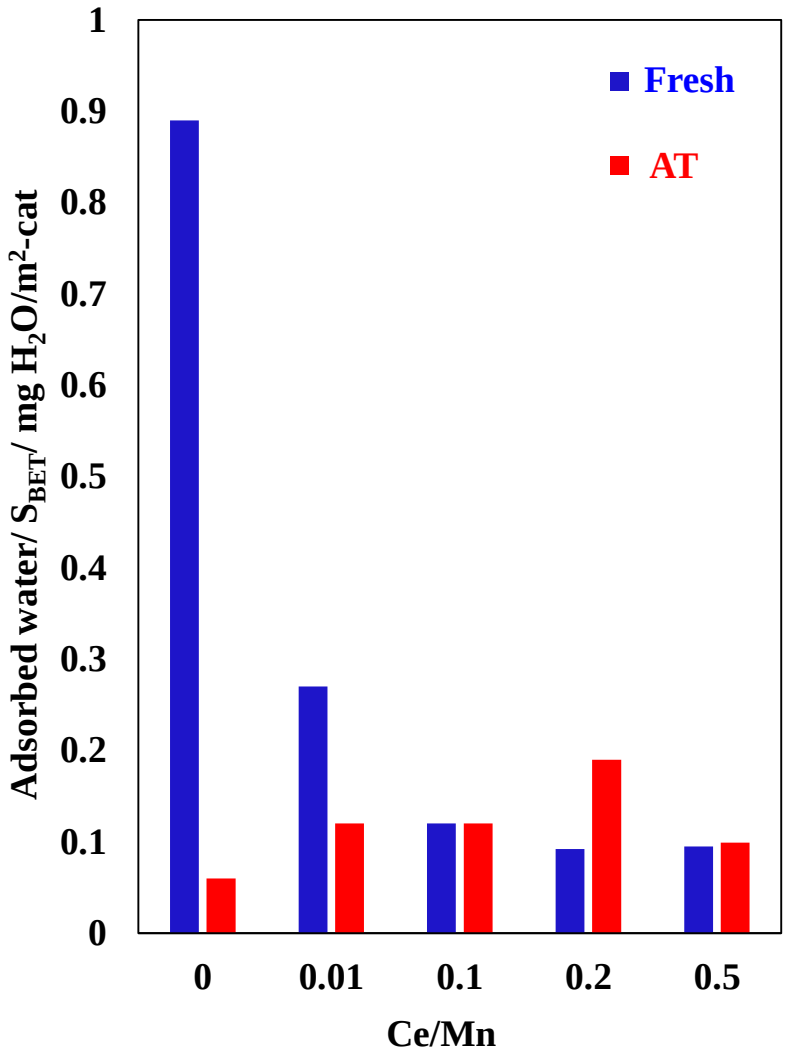
Fresh
AT
Adsorbed water/ S_{BET}/ mg H_2O/m^2-cat
1
0.9
0.8
0.7
0.6
0.5
0.4
0.3
0.2
0.1
0
0
0.01
0.1
0.2
0.5
Ce/Mn

Fig. 11.

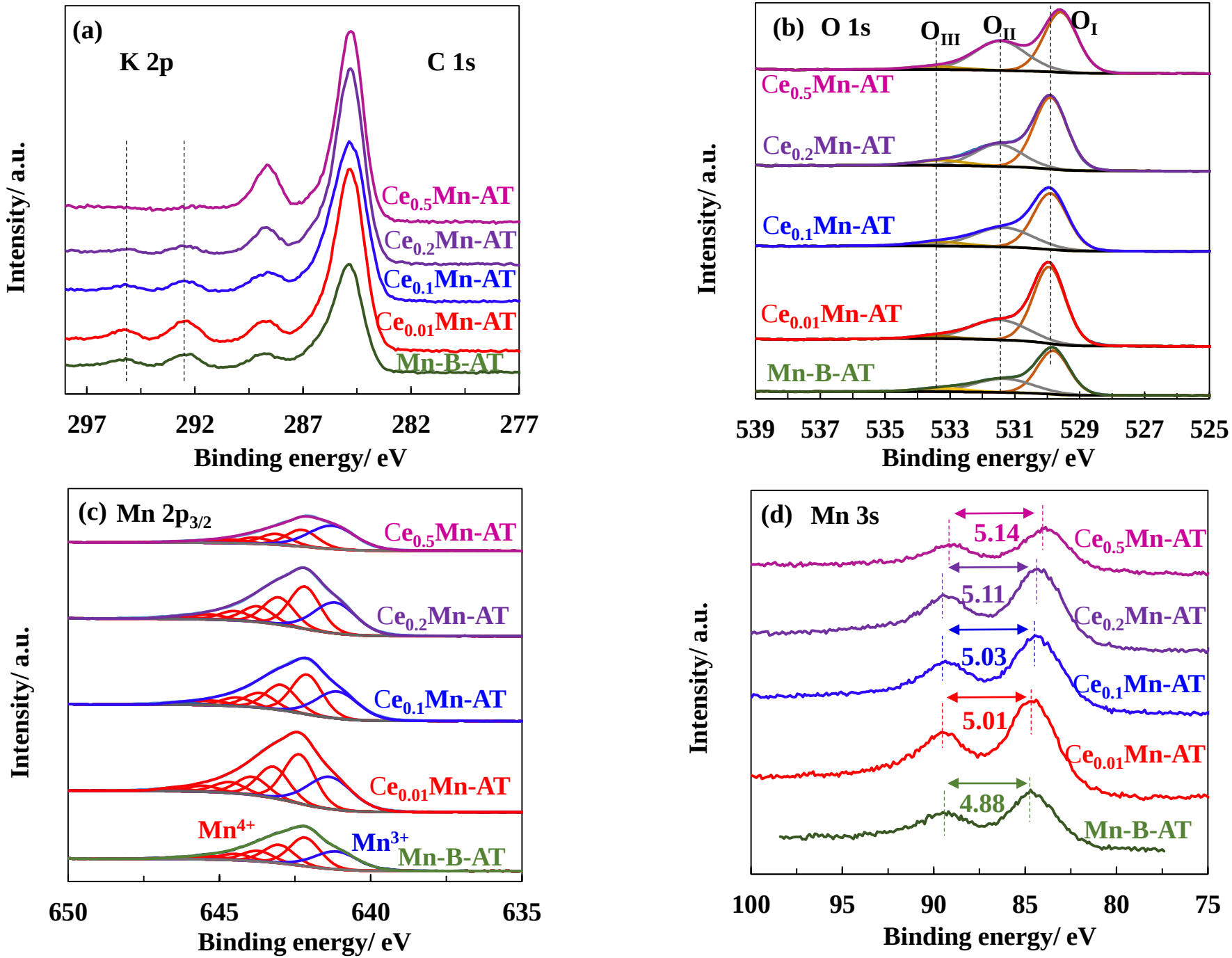
(a)
K 2p
C 1s
Intensity/ a.u.
Ce0.5Mn-AT
Ce0.2Mn-AT
Ce0.1Mn-AT
Ce0.01Mn-AT
Mn-B-AT
297
292
287
282
277
Binding energy/ eV
(b) O 1s
OIII
OII
OI
Ce0.5Mn-AT
Ce0.2Mn-AT
Ce0.1Mn-AT
Ce0.01Mn-AT
Mn-B-AT
Intensity/ a.u.
539
537
535
533
531
529
527
525
Binding energy/ eV
(c) Mn 2p3/2
Ce0.5Mn-AT
Ce0.2Mn-AT
Ce0.1Mn-AT
Ce0.01Mn-AT
Mn4+
Mn3+
Mn-B-AT
Intensity/ a.u.
650
645
640
635
Binding energy/ eV
(d) Mn 3s
5.14
5.11
5.03
5.01
4.88
Ce0.5Mn-AT
Ce0.2Mn-AT
Ce0.1Mn-AT
Ce0.01Mn-AT
Mn-B-AT
Intensity/ a.u.
100
95
90
85
80
75
Binding energy/ eV

Fig. 12.

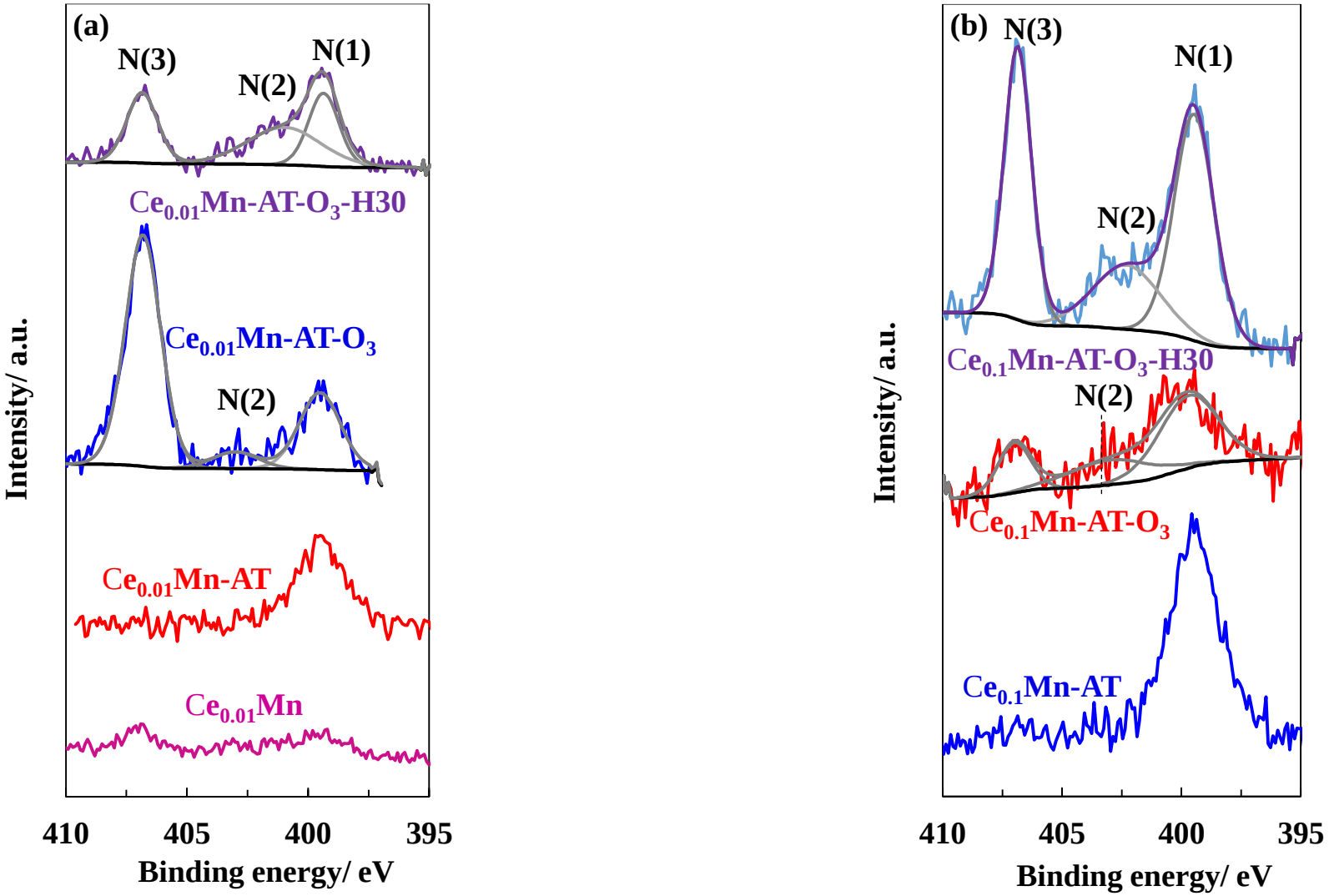
(a)
N(3)
N(2)
N(1)
Ce0.01Mn-AT-O3-H30
Ce0.01Mn-AT-O3
N(2)
Ce0.01Mn-AT
Ce0.01Mn
Intensity/ a.u.
410
405
400
395
Binding energy/ eV
(b)
N(3)
N(1)
N(2)
Ce0.1Mn-AT-O3-H30
N(2)
Ce0.1Mn-AT-O3
Ce0.1Mn-AT
Intensity/ a.u.
410
405
400
395
Binding energy/ eV

Fig. 13.

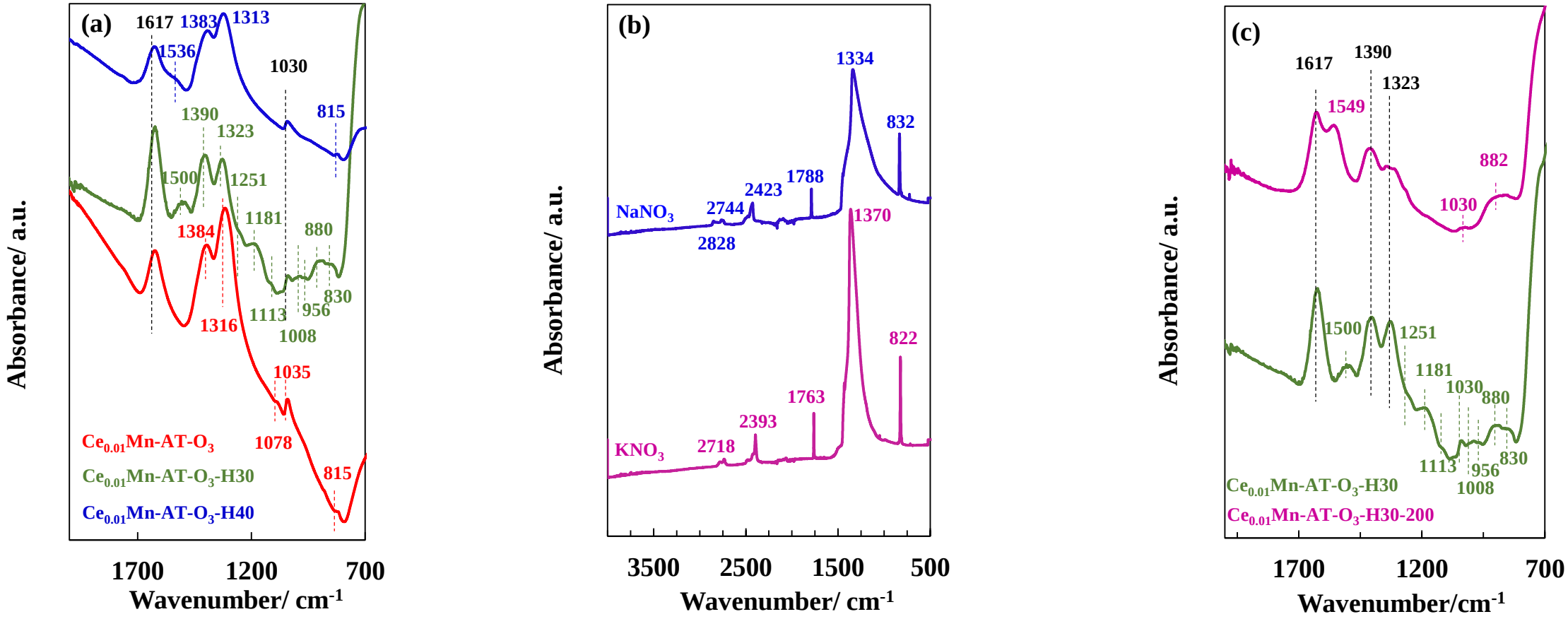
(a)
1617
1383
1313
1536
1030
815
1390
1323
1500
1251
1181
1384
880
830
956
1113
1008
1316
1035
1078
815
Ce0.01Mn-AT-O3
Ce0.01Mn-AT-O3-H30
Ce0.01Mn-AT-O3-H40
Absorbance/ a.u.
1700
1200
700
Wavenumber/ cm-1
(b)
1334
832
2423
1788
NaNO3
2744
2828
1370
822
1763
2393
KNO3
2718
Absorbance/ a.u.
3500
2500
1500
500
Wavenumber/ cm-1
(c)
1617
1390
1323
1549
882
1030
1500
1251
1181
1030
880
1113
956
830
1008
Ce0.01Mn-AT-O3-H30
Ce0.01Mn-AT-O3-H30-200
Absorbance/ a.u.
1700
1200
700
Wavenumber/cm-1

Table 1

Catalyst	ICP-EOS		Textural properties		Redox properties (H_2-TPR)		
	K/Mn	Ce/Mn	S_{BET} (m^2/g)	Vp (cm^3/g)	Tonset (°C)	n (H_2) ($mmol/g_{cat}$)	n (H_2) / n (Mn+Ce)
Mn-B-AT	0.065	-	334	0.55	140	9.20	0.90
$Ce_{0.01}Mn$-AT	0.059	0.0079	385	0.48	75	9.17	0.96
$Ce_{0.1}Mn$-AT	0.024	0.054	337	0.37	110	8.69	0.81
$Ce_{0.2}Mn$-AT	0.014	0.097	280	0.65	115	7.53	0.78
$Ce_{0.5}Mn$-AT	0.0025	0.65	355	0.26	150	2.03	0.19

Table 2

	Mn-B	$Ce_{0.01}Mn$	$Ce_{0.1}Mn$	$Ce_{0.2}Mn$	$Ce_{0.5}Mn$
Fresh	39.4	34.6	28.5	24.7	23.8
AT	21.3	48.2	40.9	53.0	35.3

Table 3

Catalyst	K/Mn	Ce/Mn	N/Mn	Mn^{3+}/Mn^{4+}	$O_I/(O_I+O_{II})$	ΔE Mn 3s (Mn AOS)
Mn-B-AT	0.04	-	0.03	0.36	0.41	4.92 (3.41)
$Ce_{0.01}Mn$-AT	0.06	0.018	0.05	0.38	0.31	5.01 (3.32)
$Ce_{0.1}Mn$-AT	0.04	0.078	0.06	0.39	0.37	5.08 (3.23)
$Ce_{0.2}Mn$-AT	0.02	0.12	0.05	0.41	0.30	5.15 (3.16)
$Ce_{0.5}Mn$-AT	-	0.78	0.07	0.87	0.37	5.14 (3.16)

Table 4

Catalyst	$MnOH^+/MnO^+$	$CeOH^+/CeO^+$	$CeMnOH^+/CeOMn^+$	$CeMnOH^+/(CeO^+ + MnO^+)$
$Ce_{0.01}Mn$	1.05	0.035	0.17	0.0027
$Ce_{0.01}Mn$-AT	3.04	0.036	1.15	0.0055
$Ce_{0.1}Mn$	1.62	0.020	0.16	0.0049
$Ce_{0.1}Mn$-AT	2.36	0.034	0.74	0.0047

Table 5

Catalyst	Position (eV)			% atom			N/Mn	$(N/Mn)_c$
	N (1)	N (2)	N (3)	N (1)	N (2)	N (3)		
Mn-B-AT-O_3	399.5	401.5	406.8	18.7	18.1	63.2	0.12	0.09
$Ce_{0.01}$Mn-AT-O_3	399.5	403.0	406.8	26.3	6.3	67.4	0.09	0.04
$Ce_{0.01}$Mn-AT-O_3-H	399.3	401.0	406.8	31.1	38.7	30.2	0.06	0.01
$Ce_{0.1}$Mn-AT-O_3	399.7	403.0	407.0	54.2	25.3	20.5	0.15	0.09
$Ce_{0.1}$Mn-AT-O_3-H	399.5	402.3	406.8	43.6	20.5	35.8	0.08	0.02
$Ce_{0.2}$Mn-AT-O_3	399.7	403.0	407.0	22.5	11.0	66.5	0.16	0.11
$Ce_{0.5}$Mn-AT-O_3	399.6	403.4	407.0	17.9	14.3	67.7	0.32	0.25

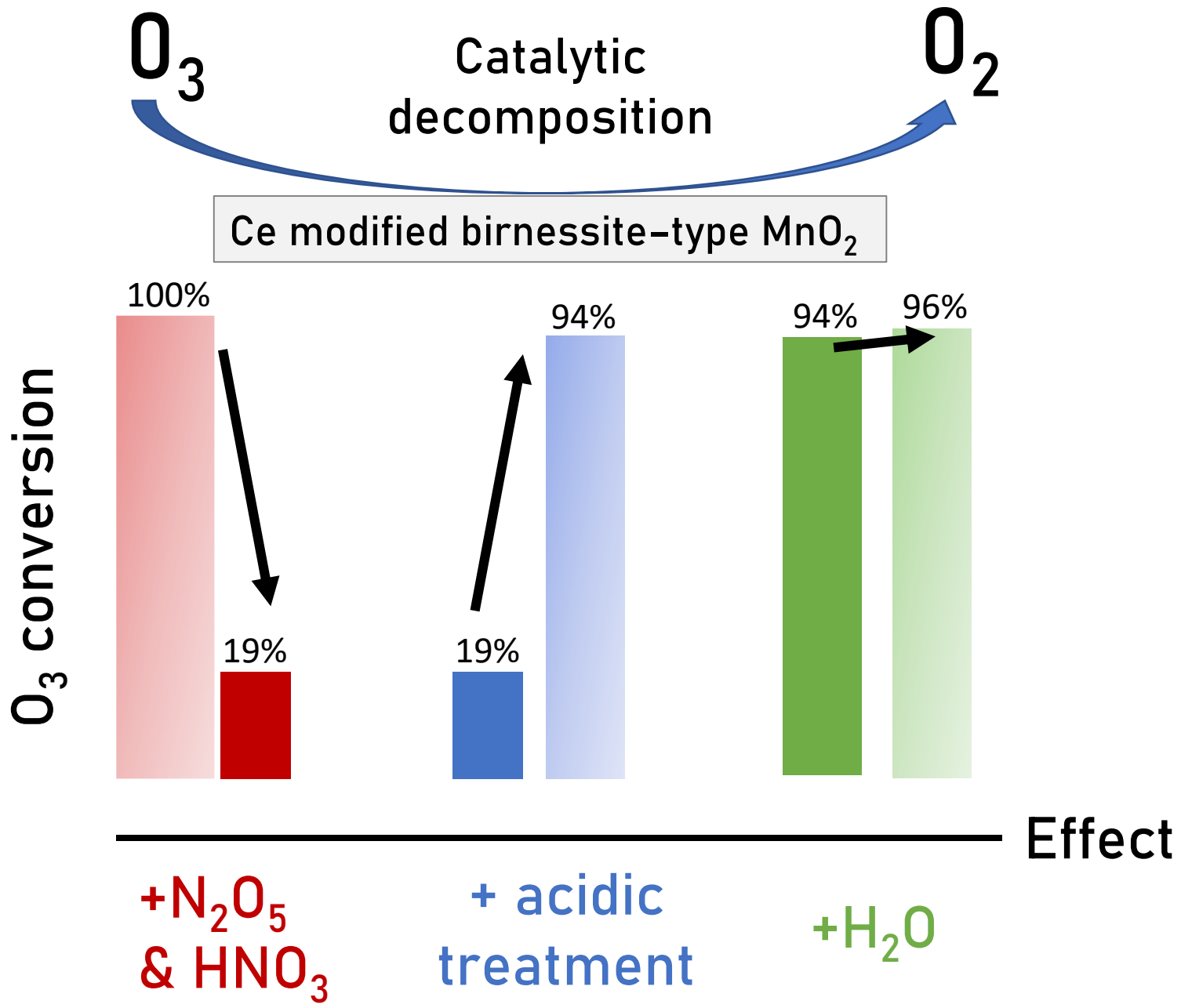
O_3
Catalytic decomposition
O_2
Ce modified birnessite-type MnO_2
100%
19%
19%
94%
94%
96%
O_3 conversion
Effect
+N_2O_5 & HNO_3
+ acidic treatment
+H_2O